



Ray theory for elastic wave propagation in graded metamaterials

Charles Dorn, Dennis M. Kochmann*

Mechanics & Materials Lab, Department of Mechanical and Process Engineering, ETH Zürich, 8092 Zürich, Switzerland

ARTICLE INFO

Keywords:

Metamaterial
Ray tracing
Waveguide
Dispersion relation
Elasticity
Finite element method

ABSTRACT

We present a ray theory for modeling elastic wave propagation in spatially graded mechanical metamaterials. Wave propagation in periodic metamaterials has been well studied, motivated by their beneficial wave steering and bandgap properties. By contrast, comparably little work has explored wave propagation in spatially graded metamaterials despite the increased design opportunities, largely due to the lack of efficient modeling techniques. We develop a ray theory to model waves in graded metamaterials based on high-frequency asymptotics and the assumption of local periodicity. This work builds upon the well-developed ray theories that are fundamental in a wide range of fields, from optics to seismology. Our derivations produce a practical framework for computing approximate wave fields in graded metamaterials. Ray trajectories are computed by independently solving a system of ordinary differential equations for each ray, requiring only knowledge of local dispersion relations throughout the metamaterial, which vary smoothly in space due to grading. Equations for the wave amplitude along rays are also derived in the two-dimensional setting. We show that the form of the ray tracing equations are nearly identical to those for smooth solids in seismic ray theory, with the primary difference being the dispersion relations. A numerical framework for computing ray solutions is demonstrated on a mass-spring network with analytical dispersion relations as well as a truss metamaterial that requires the numerical evaluation of dispersion relations. Through these examples, we demonstrate that ray theory provides an efficient means of studying the fascinating behavior of waves in graded metamaterials such as wave guiding along curved trajectories.

1. Introduction

Periodic metamaterials exhibit fascinating wave propagation behavior due to their ability to steer and attenuate waves. The exotic dynamic properties of periodic media were originally discovered in the context of atomic lattices, pioneered by the influential works of Bloch (1929) and Brillouin (1953). Subsequently, as manufacturing advances have allowed fabrication of metamaterials with detailed architectures, extensive research has focused on modeling and designing dynamic properties of periodic mechanical metamaterials (Hussein et al., 2014; Phani and Hussein, 2017), based on the periodic assembly of a unit cell composed of trusses, plates, shells, or composite materials. Of course, the design space of metamaterials extends far beyond periodic architectures. Graded metamaterials, with spatially varying unit cells, can be easily manufactured, yet have remained largely unexplored in the context of wave propagation.

For static applications, spatial grading of metamaterials has proven to be a powerful design concept to conceive materials and structures with locally optimal mechanical properties (Liu et al., 2017; Panesar et al., 2018; Sanders et al., 2021; Telgen et al., 2022). Additionally, spatial grading enables enhanced wave guiding capabilities at long wavelengths (with respect to the unit cell length

* Corresponding author.

E-mail address: dmk@ethz.ch (D.M. Kochmann).

<https://doi.org/10.1016/j.jmps.2022.105049>

Received 30 June 2022; Received in revised form 20 August 2022; Accepted 21 August 2022

Available online 28 August 2022

0022-5096/© 2022 The Author(s). Published by Elsevier Ltd. This is an open access article under the CC BY license (<http://creativecommons.org/licenses/by/4.0/>).

scale), which has been demonstrated for cloaking applications (Nassar et al., 2019; Kadic et al., 2020; Chen et al., 2021). However, the extreme attenuation and directionality of energy flow, hallmark to metamaterials, typically occurs at short wavelengths on the unit cell scale.

Past studies suggest graded metamaterials can be used to achieve wave propagation properties out of reach of periodic metamaterials, such as broadband attenuation and lensing in both the one-dimensional (Chaplain et al., 2020b; Banerjee et al., 2017; Cherednichenko, 2018; Alshaqqaq et al., 2022) and two-dimensional settings (Trainiti et al., 2016, 2018; Aguzzi et al., 2022; Wang et al., 2021; Chaplain et al., 2020a). The design space of graded metamaterials, however, remains largely unexplored in the context of short-wavelength wave propagation, as most existing research has relied on intuitive design. This is due to a lack of efficient modeling tools to explore the design space. In the static and long-wavelength regimes, past work primarily relied on classical homogenization techniques to efficiently model and design spatial grading in metamaterials, which break down for short wavelengths, though some high-frequency homogenization methods are capable of approximating dispersion relations about a given frequency (Craster et al., 2010; Nolde et al., 2011; Colquitt et al., 2015). Bloch wave analysis, which is the foundation for studying waves in periodic media, relies on the assumption of periodicity and does not directly apply to graded architectures. Direct dynamic simulations (e.g., using finite elements) require high spatial and temporal resolutions to resolve high frequency waves while capturing spatially varying unit cells, which is inefficient for inverse design problems.

To address this gap in modeling capabilities, we develop ray theory as a tool for efficiently and accurately modeling wave propagation in spatially graded mechanical metamaterials. Ray theory is a classical approximation for wave propagation, originally developed in the context of optics, where it is known as geometric optics (Born and Wolf, 2013), which was formalized by Hamilton (1828). Subsequently, it has emerged as a powerful tool for approximating wave propagation in a wide breadth of fields, from quantum mechanics (Berry and Mount, 1972) to cosmology (Isaacson, 1968) to fluid mechanics (Jensen et al., 2011). Specifically in solid mechanics, ray theory is most well known as a foundation for classical seismology (Cerveny, 2001; Chapman, 2004), dating at least to the early 1900s (see, e.g., the review by Ben-Menahem, 1995). It has also provided a useful method for studying waves in shells (Norris and Rebinsky, 1994; Mazzotti et al., 2022) and beams (Pierce, 1970).

There is a general procedure for developing ray theory in any context. First, an asymptotic analysis of the governing wave equation is performed in the limit of high frequencies and short wavelengths; this is known as the eikonal approximation, Wentzel–Kramers–Brillouin (WKB) approximation, or geometric optics approximation, depending on the field (Thorne and Blandford, 2017). This approximation yields the *eikonal* equation, a partial differential equation that can be efficiently solved along characteristic trajectories, or *rays*. A key feature of ray theory is its capability to efficiently approximate wave solutions in heterogeneous media, which motivates its popularity in such a wide range of fields.

Despite the clear demonstration of ray theory as a powerful and mature tool across many fields, it has not yet been practically applied in the context of mechanical metamaterials, though some research has applied ray tracing in the context of graded optical metamaterials (Russell and Birks, 1996, 1999; Jiao et al., 2004; Cassan et al., 2011; Cassan and Do, 2011). Ray approximations have also been developed for X-ray propagation through crystal lattices (Kato, 1963; Authier, 2004).

Building from the mathematical work of Bensoussan et al. (1978), Allaire et al. (2011), Schnitzer (2017) on asymptotic analysis of Bloch waves, we develop a practical framework for ray tracing in graded metamaterials. We approximate the graded metamaterials as locally periodic, with unit cells that change slowly in space. Ray tracing equations are derived, which consist of a system of first-order ordinary differential equations that can be solved independently for each ray to calculate its trajectory. Additionally, equations are derived to compute the wave amplitude along each ray, taking inspiration from analogous solutions in seismic ray theory (Cerveny, 2001). This leads to an efficient framework for approximating wave solutions; ray paths are computed by solving small first-order differential equation systems, while amplitudes and phases along each ray are computed simply by evaluating their derived formulas.

While we take inspiration from ray theories in optics and seismology, our work is distinct from these theories. In contrast to the optical case involving scalar waves, the elastic case we consider involves vector-valued displacement fields, which adds complexity. Seismic ray theory also studies elastic waves, but in the context of *locally homogeneous solids*, whereas we consider *locally periodic media* that exhibit dispersion due to their microstructure. The assumptions of seismic ray theory are valid for wavelengths that are much shorter than the length scale of inhomogeneity but much longer than the length scale of the microstructure. Our ray theory for locally periodic media is a generalization of seismic ray theory, which is also valid for wavelengths on (and shorter than) the length scale of the microstructure.

Based on the above theory, we implement a numerical ray tracing framework, which is demonstrated for a periodic and graded mass–spring network as well as for a truss metamaterial modeled by beam finite elements. Results demonstrate close agreement between the ray solutions and direct finite element simulations. Due to the efficiency of ray tracing, it is a promising tool for exploring the design space of spatial grading. We anticipate that it will open doors to the inverse design of spatial grading for wave manipulation, motivated by applications such as energy harvesting (De Ponti, 2021) and signal processing (Mohammadi and Adibi, 2011).

The remainder of this paper is organized as follows: Section 2 reviews elastic wave propagation in periodic media and defines the assumptions of local periodicity. Section 3 derives ray theory for locally periodic media and outlines a numerical implementation. Section 4 presents examples of ray solutions for a mass–spring network and a truss metamaterial in comparison to finite element simulations. Finally, Section 5 concludes our study.

2. Preliminaries

We consider small-amplitude elastic waves propagating in a continuum, which are described by the linear elastodynamic equation

$$\rho \ddot{u}_i = \frac{\partial}{\partial x_j} \left(C_{ijkl} \frac{\partial u_k}{\partial x_l} \right), \quad (1)$$

where the vector-valued displacement field $\mathbf{u}(\mathbf{x}, t) : B \times \mathbb{R} \rightarrow \mathbb{R}^d$ is a function of the spatial coordinate $\mathbf{x} \in B$ and time t , defined over a body $B \subset \mathbb{R}^d$ in d spatial dimensions. $\rho(\mathbf{x})$ denotes the (position-dependent) material density, and $C(\mathbf{x})$ is the fourth-order elasticity tensor. Einstein's summation convention is used throughout this paper.

2.1. Waves in periodic media

Elastic waves in periodic media have been well studied, which we briefly review here. For periodic media, the material properties $\hat{\rho}$ and \hat{C} are periodic based on unit cell domain Ω . Within a unit cell, displacements are assumed to be plane waves of the form

$$\mathbf{u}(\mathbf{x}, t) = \hat{\mathbf{A}} e^{i(\mathbf{k} \cdot \mathbf{x} - \omega t)}, \quad (2)$$

where $i = \sqrt{-1}$ is the imaginary number, $\mathbf{k} \in \mathbb{R}^d$ is the wave vector, $\omega \in \mathbb{R}$ is the frequency, and $\hat{\mathbf{A}} \in \mathbb{C}^d$ is the complex amplitude vector, which is periodic with domain Ω . Generally, the wave vector can be complex, with its imaginary part associated with material damping. However, for non-dissipative elastic materials, the imaginary part of the wave vector can be non-zero in the presence of interfaces where evanescent waves form (Srivastava and Willis, 2017; Lustig et al., 2019). In the following, we consider linear elastic materials with no material dissipation and we do not consider interfaces, so that \mathbf{k} is real throughout this paper.

The displacements within one unit cell can be directly related to the displacements in any other unit cell by Bloch's theorem (Brillouin, 1953), so only a single unit cell needs to be considered. To obtain the solution over one unit cell, the plane-wave ansatz of Eq. (2) is inserted into Eq. (1) to obtain

$$\mathcal{L}^B[\hat{\mathbf{A}}] + \omega^2 \hat{\rho} \hat{\mathbf{A}} = \mathbf{0}, \quad (3)$$

where the Bloch operator \mathcal{L}^B has components

$$\mathcal{L}_i^B[\hat{\mathbf{A}}] = \frac{\partial \hat{C}_{ijkl}}{\partial x_j} \left(\frac{\partial}{\partial x_l} + ik_l \right) \hat{A}_k + \hat{C}_{ijkl} \left(\frac{\partial^2}{\partial x_l \partial x_j} + ik_j \frac{\partial}{\partial x_l} + ik_l \frac{\partial}{\partial x_j} - k_j k_l \right) \hat{A}_k. \quad (4)$$

Eq. (3) represents the operator form of the Bloch eigenvalue problem. A standard approach for solving the latter is by converting Eq. (3) to the weak form, applying Bloch boundary conditions, discretizing using finite elements, and solving the resulting discrete eigenvalue problem numerically. This procedure is discussed in depth in Hussein et al. (2014). The solution to the Bloch eigenvalue problem yields the *dispersion relation* $\omega(\mathbf{k})$, which relates the natural frequencies ω to the wave vector \mathbf{k} , and which provides valuable information about the nature of wave propagation through the medium. The group velocity \mathbf{V} of a given mode takes the form

$$\mathbf{V} = \frac{\partial \omega}{\partial \mathbf{k}}, \quad (5)$$

and the magnitude of the group velocity is denoted $V = \|\mathbf{V}\|$. As long as the wave vector is real, which is the case considered in this paper, the group velocity determines the direction of energy flow (Willis, 2016) and is crucial to characterizing the dynamic response of a periodic material (Zelhofner and Kochmann, 2017).

2.2. Definition of locally periodic media

Our objective is a framework for modeling elastic wave propagation in spatially graded metamaterials. Such materials are assumed to be *locally periodic*, exhibiting unit cells that vary slowly in space. In the immediate vicinity of a unit cell, the medium is effectively a periodic medium. However, the unit cell is allowed to vary slowly in space with respect to the unit cell length scale.

To formally define local periodicity, we introduce two length scales. The microscopic (unit cell) length scale is denoted $l \sim O(\epsilon)$, and the macroscopic length scale is denoted $L \sim O(1)$. The two length scales are assumed to be separated such that $l/L = \epsilon \ll 1$. Resulting from the separation of scales, two independent sets of spatial coordinates are defined. Coordinate $\mathbf{X} = \mathbf{x}$ is associated with the macroscopic scale of body B , whereas coordinate $\mathbf{y} = \mathbf{x}/\epsilon$ is associated with the microscopic scale of unit cell Ω . An illustration of a locally periodic material is shown in Fig. 1, with the two coordinate systems highlighted.

In a locally periodic material, the unit cell is allowed to vary on the macroscopic length scale, but can be treated as approximately periodic on the microscopic length scale. The material properties can hence be modeled as \mathbf{y} -periodic with a small perturbation associated with spatial variations on the macroscopic length scale, which take the form

$$\begin{aligned} C(\mathbf{X}, \mathbf{y}) &= \hat{C}(\mathbf{y}) + \epsilon^2 \tilde{C}(\mathbf{X}, \mathbf{y}), \\ \rho(\mathbf{X}, \mathbf{y}) &= \hat{\rho}(\mathbf{y}) + \epsilon^2 \tilde{\rho}(\mathbf{X}, \mathbf{y}). \end{aligned} \quad (6)$$

Here, the elastic tensor and density consist of \mathbf{y} -periodic terms \hat{C} and $\hat{\rho}$, perturbed by non-periodic terms \tilde{C} and $\tilde{\rho}$. In a periodic medium the latter two would vanish. We carefully choose to consider small perturbations on the order of ϵ^2 , which leads to the

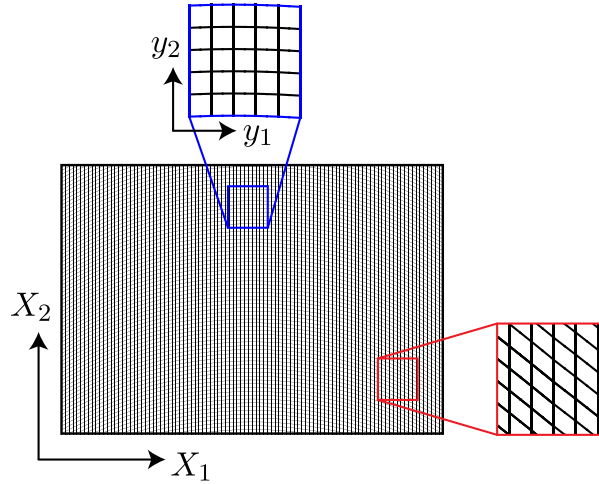


Fig. 1. Illustration of a spatially graded metamaterial, which is modeled as locally periodic with two length scales. The macroscopic coordinates X are associated with the length scale of spatial grading. The microscopic coordinates y are associated with the length scale of the unit cell.

simplest possible ray approximation. Perturbations of order ϵ could be considered but would complicate the ray equations, as discussed in Appendix A. Further discussion of the perturbation order can also be found in Allaire et al. (2011). Resulting from the assumed form of material properties in Eq. (6), solutions to the elastodynamic equation are derived and exemplified in the following.

3. Ray theory for locally periodic media

We proceed by developing ray theory for locally periodic elastic media. First, an asymptotic analysis of the elastodynamic wave equation is performed under the assumption of local periodicity to derive the eikonal equation, which governs high frequency, short-wavelength wave propagation. Solutions to the eikonal equation are obtained along rays. Ray trajectories are tangent to the group velocity and represent directions of energy flow.

3.1. Asymptotic analysis

To formulate an asymptotic approximation of the elastodynamic equation for short wavelengths and high frequencies, we begin with an ansatz for the displacements. Following the work of Bensoussan et al. (1978) and Allaire et al. (2011), the displacement field in locally periodic media is assumed to take the form

$$u(\mathbf{X}, \mathbf{y}, t) = \mathbf{A}(\mathbf{X}, \mathbf{y})e^{i\varphi(\mathbf{X}, t)/\epsilon}, \tag{7}$$

which is analogous to the plane-wave ansatz of Eq. (2), except the amplitude and phase are allowed to slowly vary, so it represents a ‘locally plane wave’. The phase $\varphi(\mathbf{X}, t)$ is assumed to vary only on the macroscopic length scale. Since this form of solution locally approximates a plane wave, the partial derivatives of the phase give the wave vector and frequency, respectively:

$$\begin{aligned} \mathbf{k} &= \frac{\partial \varphi}{\partial \mathbf{X}}, \\ \omega &= -\frac{\partial \varphi}{\partial t}. \end{aligned} \tag{8}$$

The amplitude \mathbf{A} , like the material properties, is assumed to be approximately \mathbf{y} -periodic (consisting of a periodic term plus a small perturbation), so

$$\mathbf{A}(\mathbf{X}, \mathbf{y}) = \hat{\mathbf{A}}(\mathbf{X}, \mathbf{y}) + \epsilon^2 \tilde{\mathbf{A}}(\mathbf{X}, \mathbf{y}). \tag{9}$$

Here, $\hat{\mathbf{A}}$ is \mathbf{y} -periodic, and $\tilde{\mathbf{A}}$ is a non-periodic perturbation.

Inserting the displacement ansatz of Eq. (7) into the elastodynamic wave equation, Eq. (1), the leading order terms take the form

$$\mathbf{0} = \epsilon^{-2} \mathbf{L}e^{i\varphi/\epsilon} + \epsilon^{-1} \mathbf{M}e^{i\varphi/\epsilon} + O(\epsilon^0), \tag{10}$$

where the leading term involves vector \mathbf{L} with components

$$L_i = \hat{C}_{ijkl}(-\hat{A}_k k_j k_l + i\hat{A}_{k,y_l} k_j + i\hat{A}_{k,y_j} k_l + \hat{A}_{k,y_j y_l}) + \hat{C}_{ijkl,y_j}(\hat{A}_{k,y_l} + i\hat{A}_k k_l) + \omega^2 \hat{\rho} \hat{A}_i \tag{11}$$

and the second term features

$$M_i = \hat{C}_{ijkl}(i\hat{A}_{k,X_j}k_l + i\hat{A}_{k,X_l}k_j + \hat{A}_{k,X_jy_l} + \hat{A}_{k,X_ly_j} + i\hat{A}_k k_l X_j) + \hat{C}_{ijkl,y_j}\hat{A}_{k,X_l} \tag{12}$$

A derivation of the two leading terms is presented in Appendix A. To avoid ambiguity, we employ the notation $(\cdot)_{,y_i} = \frac{\partial(\cdot)}{\partial y_i}$ and $(\cdot)_{,X_i} = \frac{\partial(\cdot)}{\partial X_i}$, which is used from here on.

All terms of order ϵ^0 or smaller are neglected, which results in *zeroth-order ray theory*. More terms of the asymptotic expansion can be accounted for to obtain higher-order theories. In seismology, higher-order ray approximations have been developed but, due to the simplicity and accuracy of zeroth-order ray theory, higher-order ray approximations are often avoided (Cerveny, 2001). Thus, following the insights from seismic ray theory, we develop the analogous zeroth-order ray theory for locally periodic media.

From the asymptotic form of the elastodynamic equation, Eq. (10), the leading two terms are associated with different scales and must vanish independently. That is, $L = 0$ and $M = 0$ must both be satisfied. We first consider solutions to $L = 0$, which allows for the computation of ray trajectories and the phase along those. Then, the amplitude along the rays results from solving $M = 0$. Together, these first two asymptotic terms provide an elegant solution for both the amplitude and phase of waves along ray trajectories.

3.2. Ray tracing system

Using the definition of the Bloch operator of Eq. (4) in Eq. (11), enforcing $L = 0$ can be written as

$$L^B[\hat{A}] + \omega^2 \hat{\rho} \hat{A} = 0. \tag{13}$$

This is identical to the periodic Bloch eigenvalue problem in the limit $\epsilon \rightarrow 0$, so the periodic case is recovered. In the case of small $\epsilon > 0$ (i.e., in the locally periodic case), the dispersion relations are obtained at each point by assuming periodicity, but the dispersion relations can vary with X . Furthermore, the analogous equation of seismic ray theory is recovered, if the unit cell is a homogeneous material where y -derivatives in L^B vanish. In this case, Eq. (13) reduces to the Christoffel equation, $\hat{C}_{ijkl}k_j k_l \hat{A}_k - \omega^2 \hat{\rho} \hat{A}_i = 0$, which governs seismic ray theory; see Section 2.4.3 of Cerveny (2001).

The resulting eigenvalues of the local Bloch eigenvalue problem in Eq. (13) take the form

$$\omega_m = \omega_m(k, X), \tag{14}$$

where m specifies the mode. This represents the *local* dispersion relation, relating wave vector k to a set of natural frequencies ω_m at a given point $X \in B$.

Let us define the mode shape within the unit cell as $g : \Omega \rightarrow \mathbb{C}^d$, which is generally complex-valued and the eigenfunction corresponding to eigenvalue ω in the eigenvalue problem of Eq. (13). The mode shape captures the variation of the complex amplitude through a given unit cell and varies only with y . We define the mode shapes as mass-normalized, such that

$$\int_{\Omega} \hat{\rho} g^* g \, dy = 1, \tag{15}$$

where $(\cdot)^*$ denotes the conjugate transpose. The reason we define the mode shapes as mass-normalized is to ensure a proper scaling of the Green's function introduced in Section 3.5, consistent with Langley (1996).

Using Eq. (8), the dispersion relation of Eq. (14) can be written as

$$\frac{\partial \varphi}{\partial t} + \omega \left(\frac{\partial \varphi}{\partial X}, X \right) = 0. \tag{16}$$

This is known as the *eikonal equation*. Each mode has its respective eikonal equation, and we have dropped the index m of the mode. The eikonal equation can be solved along its characteristics, or *rays*, which are the solution of the ray tracing system, which takes the form (Bleistein, 2012)

$$\frac{dX}{dt} = \frac{\partial \omega}{\partial k} \Big|_X = V, \tag{17a}$$

$$\frac{dk}{dt} = - \frac{\partial \omega}{\partial X} \Big|_k. \tag{17b}$$

The first equation states that the group velocity is tangent to the ray, while the second equation describes the evolution of the wave vector along the rays. Together, Eqs. (17a) and (17b) define a system of $2d$ (where d is the number of spatial dimensions) coupled first-order ordinary differential equations that determine the ray paths and wave vectors along the ray paths.

The ray tracing system is identical to that found in ray theories of other fields, such as optics and seismology (Thorne and Blandford, 2017), with the differences stemming only from the dispersion relations themselves (which are to be obtained at every point $X \in B$ from application of Bloch's theorem to the local unit cell). Additionally, the eikonal equation and its respective ray tracing system are structured identically to the Hamilton–Jacobi equations, with the dispersion relation acting as a Hamiltonian that determines the ray trajectory.

Once the ray path is known, the phase φ along the ray can be computed as follows. Since the phase is a function of X and t only, the total derivative of the phase along the ray is

$$\frac{d\varphi}{dt} = \frac{\partial \varphi}{\partial t} + V \cdot \frac{\partial \varphi}{\partial X} = -\omega + V \cdot k. \tag{18}$$

This equation can be integrated using the solution of the ray tracing system in Eqs. (17), which provides the wave vector along the ray, at which the group velocity can be evaluated. Additionally, the frequency ω along a ray is constant as long as the dispersion relation is time-invariant (Thorne and Blandford, 2017), which is generally the case for elastic media.

3.3. Transport equation

To determine the wave amplitude along a ray, we follow the work of Bensoussan et al. (1978) and Allaire et al. (2011) and express the complex amplitude of a given mode as

$$\hat{A}(X, \mathbf{y}) = a(X)g(\mathbf{y}), \quad (19)$$

where $a \in \mathbb{C}$ is the amplitude of the mode, which varies on the macroscale with $X \in \mathcal{B}$.

The modal amplitude a along a ray is determined from the second leading term in the asymptotic expansion of Eq. (10), which must vanish ($\mathbf{M} = \mathbf{0}$). Our derivation follows a similar path to that used in seismic ray theory (Cerveny, 2001), which begins by computing the scalar product

$$M_i g_i = \hat{C}_{ijkl} \left(i a_{,X_j} g_k k_l + i a_{,X_l} g_k k_j + a_{,X_j} g_{k,y_l} + a_{,X_l} g_{k,y_j} \right) g_i + \hat{C}_{ijkl,y_j} a_{,X_l} g_k g_i + i \hat{C}_{ijkl} k_{l,X_j} a g_k g_i = 0. \quad (20)$$

Utilizing the symmetry of the elasticity tensor, $\hat{C}_{ijkl} = \hat{C}_{klij}$, this becomes

$$a_{,X_l} \left[\left(\hat{C}_{ijkl} g_i g_k \right)_{,y_j} + 2i k_j \hat{C}_{ijkl} g_i g_k \right] + i a \hat{C}_{ijkl} k_{j,X_l} g_i g_k = 0. \quad (21)$$

Inserting Eq. (B.4) for group velocity (derived in Appendix B) leads to the significantly simplified equation

$$a_{,X_l} 2\hat{\rho}\omega V_l + a(\hat{\rho}\omega V_l)_{,X_l} = 0. \quad (22)$$

Finally, after multiplying both sides by a and noting that ω is constant along a ray, we arrive at

$$(a^2 \hat{\rho} V_l)_{,X_l} = 0. \quad (23)$$

This is known as the *transport equation*. It governs how the amplitude a of a given mode evolves along a ray. This is identical to the transport equation in seismic ray theory (Cerveny, 2001). If a homogeneous unit cell is considered, seismic ray theory is recovered, since the group velocity in Eq. (B.4) reduces to the analogous group velocity for a locally homogeneous material. Since our transport equation takes the same form as in seismic ray theory, the well-developed procedures from the seismology literature can be used to solve the transport equation for ray amplitudes, which is presented in the following sections.

3.4. Solving for ray amplitudes

We solve the transport equation by considering the geometry of adjacent rays. While the derivations in previous sections are general to the three-dimensional (3D) setting, we restrict the remainder of this paper to the two-dimensional (2D) setting to simplify the computation of ray amplitudes. In addition, we consider the fundamental case of a point-source excitation and derive the amplitude and phase of the resulting waves along rays emanating from the point source.

Towards solving the transport equation, we introduce the *ray parameter* γ , which specifies a given ray based on its initial conditions. There is not a unique way to specify γ . For example, γ could represent the takeoff angle of the ray from a point source, or alternatively the angle of the initial wave vector. For the sake of consistency, we refer to γ as the *takeoff angle* from the point source. The ray path can be specified in the coordinate system (γ, s) , where s is the arc length along the ray, as well as in Cartesian coordinates (X_1, X_2) . The ray Jacobian J between the two coordinate systems is defined as

$$J = \det \begin{bmatrix} \frac{\partial X_1}{\partial \gamma} & \frac{\partial X_1}{\partial s} \\ \frac{\partial X_2}{\partial \gamma} & \frac{\partial X_2}{\partial s} \end{bmatrix}. \quad (24)$$

The transport equation is solved by examining a *ray tube*, which is illustrated in Fig. 2. A ray tube is the area enclosed by two adjacent rays with takeoff angles γ and $\gamma + d\gamma$ from a point source, between arc lengths s_r and s . The cross-sections of the ray tube are segments of length $d\ell_r^\perp$ at s_r and $d\ell^\perp$ at s , which are measured perpendicular to the ray. The area enclosed by the ray tube is denoted \mathcal{A} .

The ray cross-section is related to the Jacobian by (Cerveny, 2001)

$$d\ell^\perp = J d\gamma. \quad (25)$$

Since this identity only concerns the geometry of the ray tube, it applies to rays in both seismic media and locally periodic media.

To solve the transport equation, Eq. (23) is integrated over the area of the ray tube and the divergence theorem is applied, which leads to

$$\iint_{\mathcal{A}} \operatorname{div}_X (a^2 \mathbf{V}) d\mathcal{A} = \int_{\partial\mathcal{A}} a^2 \mathbf{V} \cdot \mathbf{n} d\ell = 0, \quad (26)$$

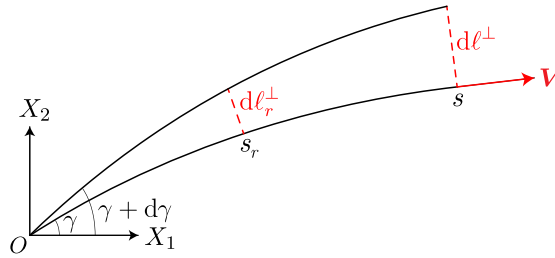


Fig. 2. Schematic of a two-dimensional ray tube. A ray emanating from a point source at the origin with takeoff angle γ is shown alongside a neighboring ray with takeoff angle $\gamma + d\gamma$.

where ∂A is the boundary of the ray tube and \mathbf{n} is the outward unit normal along the boundary. Since the group velocity \mathbf{V} is tangent to the ray, the only contributions to Eq. (26) are integrals along $d\ell^\perp$ and $d\ell_r^\perp$, so Eq. (26) simplifies to

$$\int_{d\ell_r^\perp} (a^2 \mathbf{V} \cdot \mathbf{n})_{s_r} d\ell + \int_{d\ell^\perp} (a^2 \mathbf{V} \cdot \mathbf{n})_s d\ell = 0. \tag{27}$$

This integral can be simplified further since the group velocity is parallel to \mathbf{n} along the cross-section, so that $\mathbf{V} \cdot \mathbf{n} = V$ along $d\ell^\perp$ and $\mathbf{V} \cdot \mathbf{n} = -V$ along $d\ell_r^\perp$. Eq. (26) now becomes

$$- \int_{d\ell_r^\perp} (a^2 V)_{s_r} d\ell + \int_{d\ell^\perp} (a^2 V)_s d\ell = 0. \tag{28}$$

Inserting Eq. (25) into Eq. (28), we obtain

$$\int_\gamma^{\gamma+d\gamma} \left[(a^2 V J)_s - (a^2 V J)_{s_r} \right] d\gamma = 0. \tag{29}$$

Since there is freedom in how to specify γ (e.g., as the takeoff angle from a point source or as the X_1 -component of the wave vector), the integrand of Eq. (29) must vanish, yielding

$$(a^2 V J)_s = (a^2 V J)_{s_r}. \tag{30}$$

Alternatively, this can be written as a function of time, since s can be taken as a function of time; both s and t monotonically increase along a ray. Solving for $a(t)$ yields

$$a(t) = a(t_r) \sqrt{\frac{V(t_r)J(t_r)}{V(t)J(t)}}, \tag{31}$$

which is known as the *continuation formula*. Given the ray amplitude at one location on a ray, Eq. (31) provides a simple relation to the amplitude at any other point on the ray. Computation of J is discussed in Section 3.6.

3.5. Ray amplitudes due to a point source

A fundamental and practical case that we consider is a harmonic point excitation. The continuation formula provides a means of computing the amplitude along a ray, given some known reference value. However, using a point source as a reference requires special treatment. At a point source, many rays intersect and therefore $J = 0$. Thus, a point source is a singularity of ray theory.

This singularity can be circumvented by the following procedure, which follows a similar approach in the seismology literature (Kendall et al., 1992). First, we define the limit

$$\psi_0 = \lim_{t \rightarrow 0^+} a(t) \sqrt{V(t)J(t)}, \tag{32}$$

which is taken along a given ray. Using the point source as the reference ($t_r = 0$), the continuation formula, Eq. (31), can now be written as

$$a(t) = \frac{\psi_0}{\sqrt{V(t)J(t)}}. \tag{33}$$

The value of ψ_0 cannot be determined using ray theory alone. However, while the continuation formula is generally valid for spatially varying media (since we assume local periodicity), the medium can be treated as periodic in the limit $t_0 \rightarrow 0^+$. Therefore, the Green's function for the case of an infinite 2D periodic medium is used to determine ψ_0 .

The frequency domain Green's function for 2D periodic media, which is the response of an infinite periodic medium to a harmonic point excitation, was derived by Langley (1996). In our notation, the Green's function \mathbf{u}_G takes the form

$$\mathbf{u}_G(\mathbf{X}, \mathbf{y}, \omega) = a_G(\mathbf{X}) \mathbf{g}(\mathbf{y}) e^{i(\mathbf{k} \cdot \mathbf{X} - \omega t)} \tag{34}$$

with complex amplitude

$$a_G = \frac{i\mathbf{F}^T \mathbf{g}_0}{2\omega\sqrt{2\pi|Z|}} e^{-i\frac{\pi}{4}\text{sgn}(Z)}. \quad (35)$$

Here, $\mathbf{F} \in \mathbb{R}^3$ is a vector that provides the magnitude and direction of the harmonic force at the point source, and $\mathbf{g}_0 = \mathbf{g}(\mathbf{y}_0) \in \mathbb{C}^3$ is the mode shape evaluated at the point $\mathbf{y}_0 \in \Omega$ in the unit cell, where the point force is applied. Note that, although we limit our study to 2D spatially graded media, the applied force and resulting displacements are 3D in general (considering both in-plane and out-of-plane motion). Quantity Z is defined as

$$Z = \frac{\partial^2 \omega}{\partial k_1^2} \frac{\partial \omega}{\partial k_2} X_2 - \frac{\partial^2 \omega}{\partial k_1 \partial k_2} \left(\frac{\partial \omega}{\partial k_1} X_2 + \frac{\partial \omega}{\partial k_2} X_1 \right) + \frac{\partial^2 \omega}{\partial k_2^2} \frac{\partial \omega}{\partial k_1} X_1. \quad (36)$$

This Green's function was derived under the asymptotic assumption of high frequencies and is hence valid in the far-field. While Langley's derivation includes a damping term in the Green's function, in this derivation we neglect the contribution of damping.

With Green's function in hand, the value of ψ_0 can be determined. As the point source is approached, the ray amplitude of Eq. (33) must be equal to the Green's function amplitude of Eq. (35). Therefore,

$$\psi_0 = \frac{i\mathbf{F}^T \mathbf{g}_0 \sqrt{V_0 J_0}}{2\omega\sqrt{2\pi|Z_0|}} e^{-i\frac{\pi}{4}\text{sgn}(Z_0)}, \quad (37)$$

where index $(\cdot)_0$ indicates that a quantity is evaluated in the limit $t \rightarrow 0^+$, i.e., approaching the point source. Both J and Z vanish at the point source, but they vanish at the same rate so their quotient is a finite constant as the point source is approached. This constant is derived in Appendix C, along with the signs of J_0 and Z_0 . The resulting form of ψ_0 is

$$\psi_0 = \frac{i\mathbf{F}^T \mathbf{g}_0 \sqrt{\text{sgn}(J_0)}}{2\omega\sqrt{2\pi V_0}} \left\| \frac{\partial \mathbf{k}}{\partial \gamma} \right\|_0^{1/2} e^{-i\frac{\pi}{4}\text{sgn}(Z_0)}. \quad (38)$$

Inserting this into Eq. (33), we obtain the final result for the amplitude along a ray emanating from a point source:

$$a(t) = \frac{i\mathbf{F}^T \mathbf{g}_0}{2\omega} \left(\frac{\text{sgn}(J_0/J(t))}{2\pi V_0 V(t) |J(t)|} \left\| \frac{\partial \mathbf{k}}{\partial \gamma} \right\|_0 \right)^{1/2} e^{-i\frac{\pi}{4}\text{sgn}(Z_0)}. \quad (39)$$

This equation provides a simple tool for computing the amplitude at any point along a ray. However, the amplitude is not valid for the case of $J = 0$, which corresponds to a *caustic*, which occurs when two adjacent rays intersect and the ray tube collapses to a point. Caustics are a singularity of ray theory; the amplitude tends to infinity at a caustic, resulting from the violation of the assumption that the amplitude varies slowly in space. Away from regions near a caustic (including point sources), however, Eq. (39) provides an accurate approximation of the wave amplitude. Further discussion of caustics is presented in the context of the examples in Section 4.

3.6. Numerical implementation

This section presents a numerical implementation of the ray theory equations to approximate the wave field. We specifically consider the case of a harmonic excitation at frequency ω_f at a point source located at $\mathbf{X}_0 = \mathbf{0}$ in a 2D locally periodic medium. The objective of this numerical implementation is to obtain an approximation of the wave field that results from the harmonic excitation.

We assume that the dispersion relations $\omega(\mathbf{k}, \mathbf{X})$ are available throughout the domain either analytically (as is the case for the examples in Section 4.1) or numerically (see the examples in Section 4.2). The implementation procedure is as follows:

1. Set the initial conditions \mathbf{X}_0 and \mathbf{k}_0 for the ray tracing equations. The initial position of each ray is $\mathbf{X}_0 = \mathbf{0}$, the location of the point source. The initial wave vector \mathbf{k}_0 of a ray must lie on the $\omega_f = \omega(\mathbf{k}_0, \mathbf{X}_0)$ level set of the dispersion relation at the origin. Thus, for each mode whose dispersion surface intersects $\omega = \omega_f$, the possible values of \mathbf{k}_0 lie on the level set of the forcing frequency. To initialize many rays, the level sets of the dispersion surfaces should be densely sampled.
2. For each set of initial conditions, solve the ray tracing system, Eqs. (17), which are a system of four first-order ordinary differential equations. The solution provides the ray path $\mathbf{X}(t)$ and the wave vector $\mathbf{k}(t)$ along the ray path. Derivatives of the dispersion relation can be computed using a finite-difference scheme, if no analytical form of the dispersion relations is available.
3. Compute the phase $\varphi(t)$ along each ray, using Eq. (18), where the frequency along the ray is ω_f and the group velocity and wave vector result from the solution of the ray tracing system.
4. Compute the ray Jacobian along each ray. In our implementation, we employ a finite-difference scheme to compute J , using two adjacent rays. In the finite-difference context, Eq. (25) becomes

$$J = \frac{\Delta \ell^\perp}{\Delta \gamma}, \quad (40)$$

where $\Delta \ell^\perp$ is the length of the segment between two adjacent rays at arc length s , and $\Delta \gamma$ is the difference in takeoff angle between the two rays. The sign of $\Delta \ell^\perp$ can be determined by taking the cross-product of the group velocity (which lies tangent to the ray) and the vector connecting ray γ to ray $\gamma + \Delta \gamma$ at the given arc length.

5. Compute the amplitude along each ray. When inserting Eq. (40) and $\|\frac{\partial k}{\partial \gamma}\| = \frac{\|\Delta k\|}{|\Delta \gamma|}$ into Eq. (39), the ray amplitude in the context of finite differences is given by

$$a(t) = \frac{i\mathbf{F}^T \mathbf{g}_0 \sqrt{\|\Delta \mathbf{k}_0\| \operatorname{sgn}(J_0/J(t))}}{2\omega \sqrt{2\pi V_0 V(t) \Delta \ell^\perp(t)}} e^{-i\frac{\pi}{4} \operatorname{sgn}(Z_0)}. \quad (41)$$

This equation for the amplitude relies entirely on quantities known from the initial conditions or from the solution to the ray tracing system, so it can be directly evaluated once the ray tracing system is solved. Note that this final equation for the ray amplitude is independent of the ray parameter γ .

6. Compute the total displacement at a point by summing the displacements of all rays passing through that point,

$$\mathbf{u} = \sum_{r=1}^R a_r \mathbf{g}_r e^{i\varphi_r}, \quad (42)$$

where a_r , φ_r , and \mathbf{g}_r are, respectively, the amplitude, phase, and mode shape along ray r , while R represents the number of rays passing through point X . Generally, the computed rays will not pass through the exact same points. To circumvent this, we interpolate the quantities a_r , \mathbf{g}_r , and φ_r onto a grid in the X_1 - X_2 -plane, which allows for the summation to be taken at each grid point.

This implementation provides a simple and efficient means of computing ray approximated wave fields, with the most expensive step being the solution of the ray tracing system. Note that it is suitable for parallel implementation, since the ray tracing system can be solved independently for each ray.

There are many possible alternative implementations of ray tracing, so the above procedure provides only one option. For example, the ray tracing system could alternatively be solved as a boundary value problem, given the point source location and the desired end point of the ray. Furthermore, instead of using finite differences, the calculation of the ray Jacobian can be cast into an ODE system (known as the *dynamic ray tracing system* in seismology, see [Cerveny \(2001\)](#)). However, since the dispersion relations for mechanical metamaterials generally require a numerical evaluation in the first place, finite-difference approximations of derivatives are unavoidable, so we adopt the finite-difference Jacobian calculation of Eq. (40) for simplicity. Finally, while we only consider a harmonic point excitation, more complex load cases can be considered by superposition of point sources with varying frequencies and locations.

4. Results

4.1. Mass-spring network

The first example we present is a network of point masses connected by linear elastic springs. While being a simple toy model, this example allows us to illustrate the above ray theory in an instructive manner. Consider a rectangular grid of particles of identical masses, each connected to its neighbors in the horizontal and vertical directions as well as to the neighbors in the diagonal directions (see [Fig. 3](#)). Each mass is allowed to move in-plane with two degrees of freedom, the displacements u_1 and u_2 in the X_1 - and X_2 -directions, respectively. This mass-spring network offers a simple setting to demonstrate ray tracing since the dispersion relations are analytical, yet it is complex enough to exhibit interesting dynamic behavior.

A unit cell consists of only a single mass, and there are two modes resulting from the two degrees of freedom. The equations of motion along with analytical dispersion relations are derived in [Appendix D](#). Within this general setup, we study a periodic geometry in [Section 4.1.1](#) and a spatially graded geometry in [Section 4.1.2](#).

4.1.1. Periodic case

The periodic mass-spring network is shown in [Fig. 3](#). In this example, the spacing between all masses in both the vertical and horizontal directions is h , leading to square unit cells. All springs have the same stiffness K and all particles have mass m .

The corresponding dispersion relations are derived by examining one unit cell (a single mass) in Eq. (D.5), which are plotted in [Fig. 4](#) (normalized by the frequency scaling factor $\omega_0 = \sqrt{K/m}$). Resulting from the two degrees of freedom per unit cell, there are two dispersion surfaces corresponding to the two modes of the unit cell.

To study the response of the network to harmonic excitation at the origin, a harmonic forcing is applied at frequency $\omega_f = 1.75\omega_0$ in the X_2 -direction, so $\mathbf{F} = (0, 1)^\top$ with unit magnitude. (Since the ray amplitudes scale linearly with the forcing magnitude, we simply choose a unit magnitude without loss of generality.) As a reference for validation, we compute the direct numerical solution to the equations of motion of Eq. (D.1) on a finite grid of 200×200 masses. A snapshot of the wave field at $t = 25/\omega_f$ is shown in [Fig. 5c](#).

The first step in implementing ray tracing is to determine the initial conditions of the rays. This is achieved by taking a level set of the dispersion relations at the forcing frequency, which is illustrated in [Fig. 4](#) for both modes (see the solid lines, which are projections of the level sets into the $\omega = 0$ plane). All possible initial wave vectors lie on these level sets. To obtain initial conditions for rays spanning all directions, we densely sample these level sets to provide initial conditions for 500 rays. The next step is to solve the ray tracing system to obtain the ray trajectory and wave vector along the ray for each set of initial conditions, followed by computation of phase, Jacobian, and amplitude along each ray according to [Section 3.6](#).

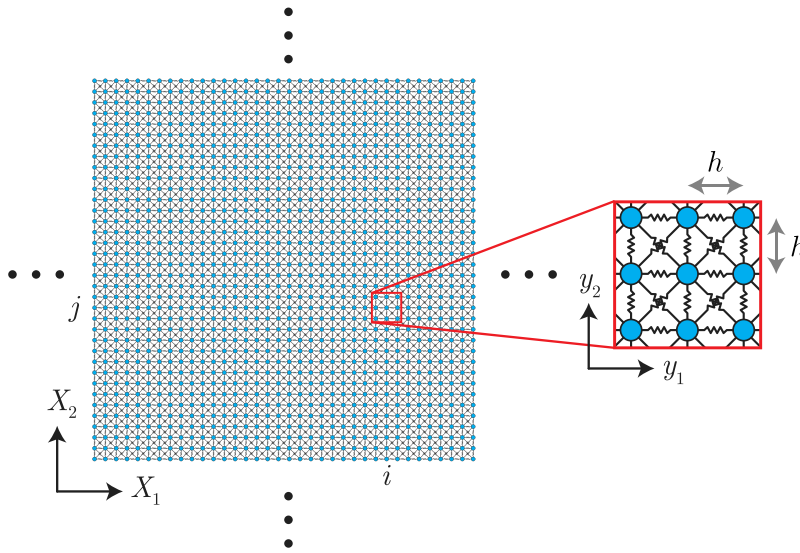


Fig. 3. Periodic mass-spring network with mass (i, j) and its neighbors highlighted.

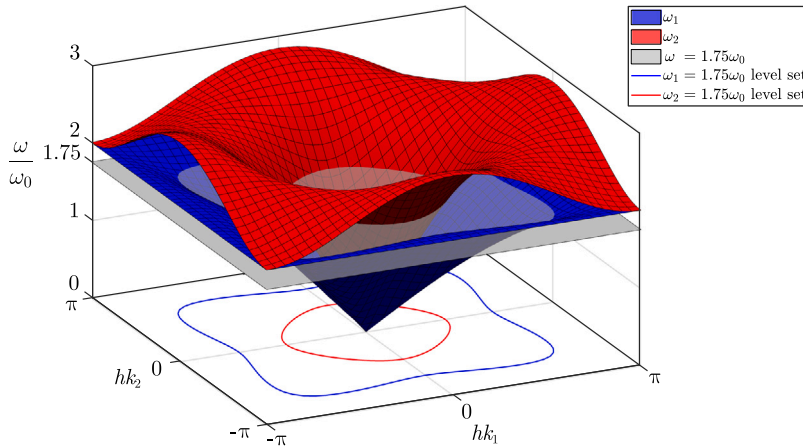


Fig. 4. Dispersion relations of the mass-spring network for the case of square unit cells with side lengths h and identical masses and spring stiffness values throughout the network.

The ray trajectories and amplitudes of both modes are plotted in Fig. 5 (in comparison to a snapshot of a discrete finite element simulation). In this example, as is the case for any periodic architecture, all rays are straight lines. This follows from Eq. (17b), since $\frac{\partial \omega}{\partial X} = 0$ in the periodic case; the wave vector is constant along the rays and therefore the group velocity, which is tangent to the ray, is also constant. Also note that the ray trajectories are *independent* of the forcing magnitude and direction and only depend on the forcing frequency ω_f . Only the amplitudes depend on the forcing F through Eq. (39) (in a linear fashion).

An interesting feature of this example is that mode 1 exhibits *multipathing*: some directions exhibit multiple overlapping rays of the same mode, which is explained as follows. In Fig. 5, nearly vertical and nearly horizontal directions exhibit multiple mode 1 rays. This phenomenon results from the shape of the dispersion surface level set in Fig. 4. The initial group velocity, which is the outward normal to this level set, is the outward normal to this level set. Since the level set of mode 1 has a non-convex shape, there can be multiple wave vectors on the level set with the same normal vector.

The displacement at a given point is obtained by summing the displacements of each ray passing through that point, according to Eq. (42). For points at which two mode 1 rays pass through, both contribute to this summation. To carry out this summation, the quantities a , φ , and g , which are defined along each ray, are interpolated onto the coordinates of each mass.

Fig. 6 shows the maximum displacement amplitude at each point between $t = 0$ and $t = 40/\omega_f$. Here, we extend the duration of the simulation compared to Fig. 5 to allow more details of the wave field to evolve. In the direct numerical simulation, reflections of mode 2 off the boundary of the grid have minimal effect since mode 2 has a very small amplitude. We do not model the boundary reflections in the ray solution.

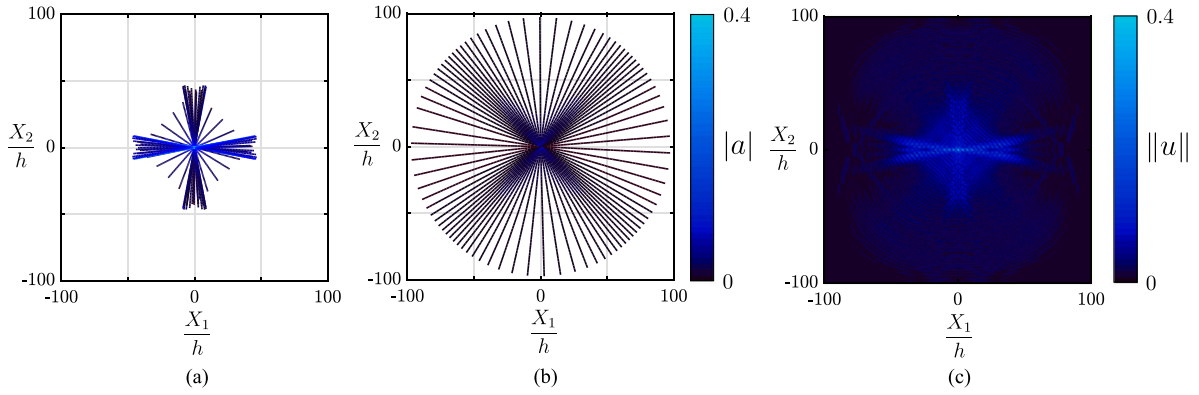


Fig. 5. Solution for the periodic mass–spring network, evaluated at $t = 25/\omega_f$. (a) Mode 1 ray paths and amplitudes (corresponding to ω_1). (b) Mode 2 ray paths and amplitudes (corresponding to ω_2). (c) Snapshot of the displacement magnitude at every point at time $t = 25/\omega_f$, as obtained from the direct numerical solution.

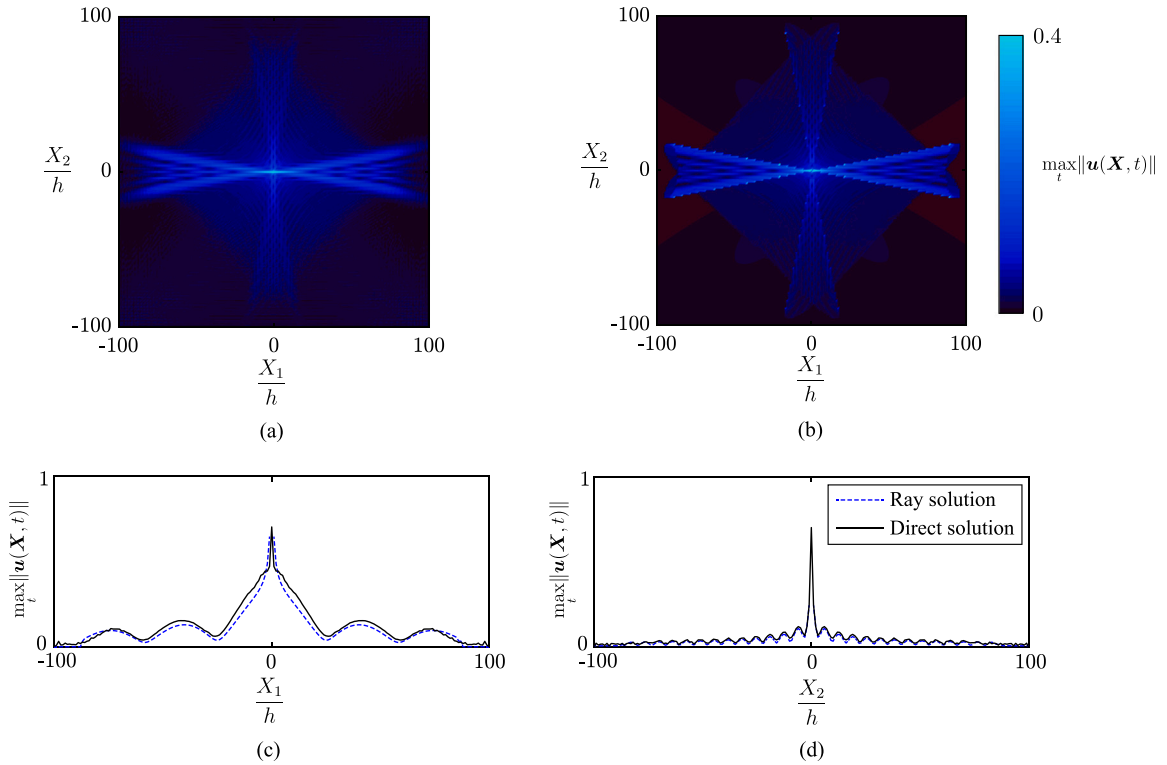


Fig. 6. Comparison of wave amplitudes for the periodic mass–spring network. At each point, the maximum displacement amplitude between $t = 0$ and $t = 40/\omega_f$ is plotted for (a) the direct numerical solution and (b) the ray solution, where all rays passing through each point have been superimposed. (c) Maximum amplitude along the X_1 -axis (at $X_2 = 0$). (d) Maximum amplitude along the X_2 -axis (at $X_1 = 0$).

The wave amplitudes in Fig. 6 show close agreement between the direct solution to the equations of motion and the ray solution. Furthermore, an intricate interference pattern is observed, which results from the superposition of waves. The ray solution offers insight into the source of these interference patterns. In the X_1 -direction, the interference pattern is caused by superposition of overlapping mode 1 rays; it appears even when mode 2 is neglected in the summation of Eq. (42). In the X_2 -direction, by contrast, the interference pattern is caused by superposition of mode 1 and mode 2 rays.

4.1.2. Graded case

To demonstrate ray tracing in a graded architecture, we modify the mass–spring network to have spatially varying unit cell dimensions. In this example, the unit cell width h_1 and height h_2 are varied linearly in space according to the functions $h_1 = CX_1 + h_0$

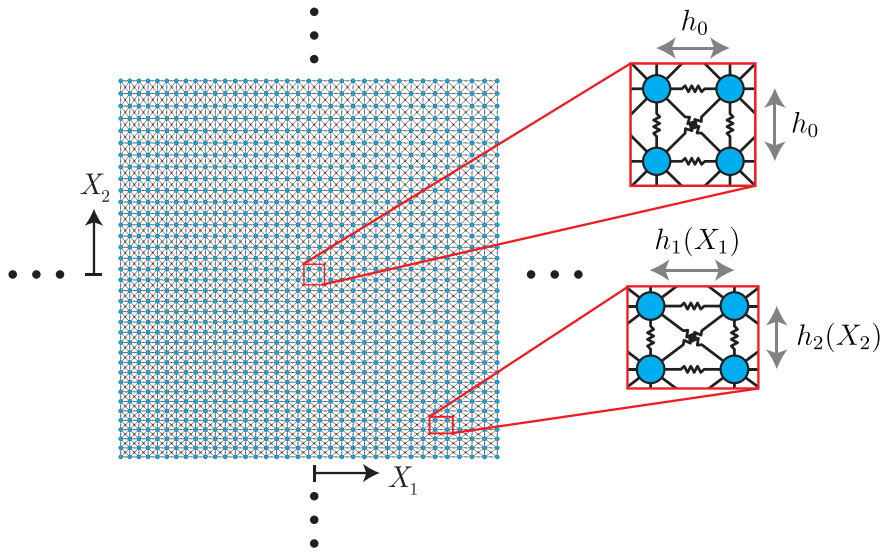


Fig. 7. Graded mass–spring network, with unit cell dimensions h_1 and h_2 graded linearly in space.

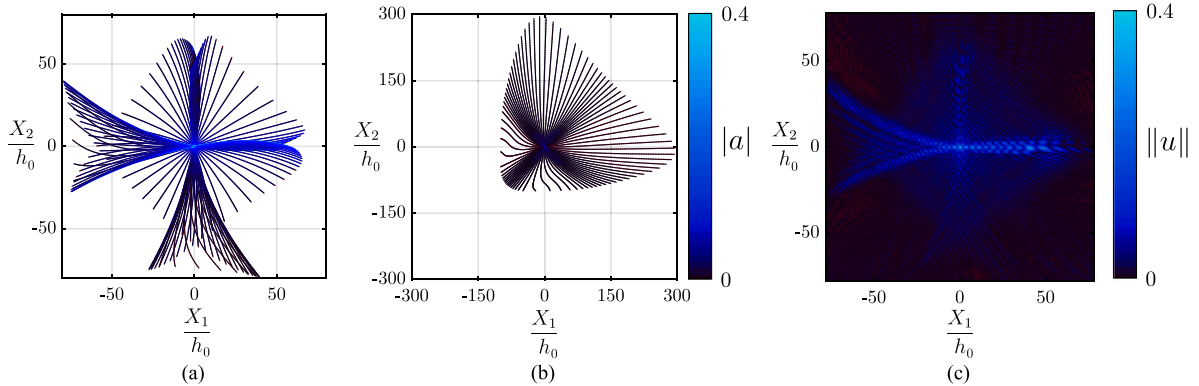


Fig. 8. Solution for the graded mass–spring network evaluated at $t = 40/\omega_f$. (a) Mode 1 ray paths and amplitudes. (b) Mode 2 ray paths and amplitudes. (c) Snapshot of the displacement magnitude of the full numerical solution. Note that the scaling of (b) is extended to fit the rays of mode 2.

and $h_2 = CX_2 + h_0$. The grading rate is taken as $C = 0.005$, and the resulting graded geometry is shown in Fig. 7. Following the periodic example, a unit harmonic force at frequency $\omega_f = 1.75\omega_0$ in the direction $F = (0, 1)^T$ is applied at the origin, while all springs have the same stiffness K , and all particles have mass m .

The initial conditions of the ray tracing system are identical to those of the periodic case. This is because the point excitation is at the origin, which has a square unit cell so the local dispersion relations correspond to Fig. 4. In the ray tracing system, the spatial derivative of the dispersion relations are obtained from the grading function as $\frac{\partial\omega}{\partial X_i} = C \frac{\partial\omega}{\partial h_i}$. Following the procedure of Section 3.6, the ray trajectories and amplitudes are computed and plotted in Fig. 8.

Owing to the spatial grading, the ray paths here follow curved trajectories. The solution shows that, in the $-X_1$ - and $-X_2$ -directions, the mode 1 rays spread out, while in the $+X_1$ - and $+X_2$ -directions the rays concentrate. For mode 1, the amplitude is highest in the $+X_1$ -direction, resulting in a strong *one-way directivity* of the wave.

For reference, a snapshot of the direct numerical solution to the equations of motion is plotted in Fig. 8c, which is computed on a grid of 200×200 masses with a fixed boundary. Again, reflections of mode 2 off the boundary are present in the direct solution at the snapshot considered, but since mode 2 has relatively small amplitude, these reflections have minimal effect on the amplitude of the solution.

In Fig. 9, the maximum displacement amplitude obtained from summing the contributions of rays is plotted alongside the maximum displacement magnitude during the direct simulation. There is a clear qualitative match between Figs. 9a and 9b. However, while Fig. 9d reveals a close quantitative match along the X_2 -direction, Fig. 9c shows larger deviations between the ray amplitude and the direct solution amplitude along the X_1 -direction. This reason for this discrepancy is the presence of *caustics*, or the self-intersection of rays. At a caustic $J = 0$, leading to a singularity in the amplitude of Eq. (39). This example features caustics

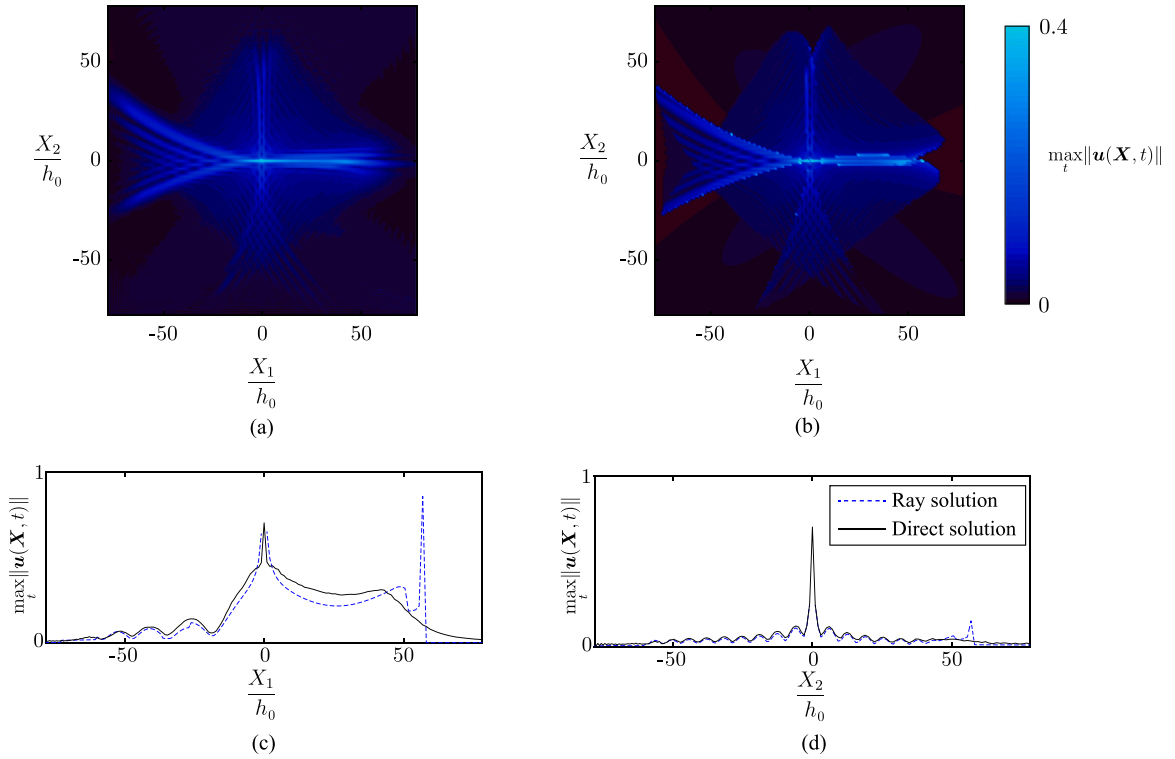


Fig. 9. Comparison of wave amplitudes for the graded mass-spring network. At each point, the maximum displacement amplitude between $t = 0$ and $t = 40/\omega_f$ is plotted for (a) the direct numerical solution and (b) the ray solution, where all rays passing through each point have been superimposed. (c) Maximum amplitude along the X_1 -axis. (d) Maximum amplitude along the X_2 -axis.

in the near-horizontal and near-vertical directions of mode 1, associated with the boundary of the region where two sets of mode 1 rays overlap. In Fig. 8a, the caustic curve intersects the X_1 - and X_2 -axes shortly after $X_1/h = 50$. While this is a clear limitation of ray theory, the ray amplitude remains valid away from caustics. Note that the ray trajectories are unaffected by caustics and remain valid at caustic points.

4.2. Graded truss metamaterial

The final example demonstrates ray tracing in a graded truss metamaterial comprised of a network of beams, which is modeled using a finite element description based on linear elastic 3D Timoshenko beam elements. While the use of finite elements creates a physically realistic problem setting, the dispersion relations must be evaluated numerically, unlike in the previous mass-spring network examples, which admitted analytical dispersion relations. Nevertheless, ray tracing can be performed based on numerically evaluated dispersion relations.

We consider a truss with quadrilateral unit cells, as shown in Fig. 10. The angle ϕ of the unit cell is spatially graded according to $\phi = DX_1/h$ with a grading rate of $D = 0.01$. The resulting geometry has a square unit at $X_1 = 0$ that grades into a parallelogram with increasing angle away from $X_1 = 0$. Each unit cell edge is a beam with a circular cross-section of diameter $0.1h$. An out-of-plane harmonic excitation is applied to the origin.

The local dispersion relations (a different set of dispersion relations for each unit cell) are computed based on a finite element model of a unit cell. Timoshenko beam elements are used with a density of 10 elements per unit cell edge. Bloch boundary conditions are applied to the unit cell, and the dispersion relations are computed by solving an eigenvalue problem for a given wave vector k . A detailed discussion of dispersion relation computations for 2D truss networks was presented by, e.g., Zelhofer and Kochmann (2017).

For ray tracing, the dispersion relations are needed for all unit cells present in the truss. To set up the ray tracing system, dispersion relations are pre-computed over a grid in k -space covering the first Brillouin zone for a set of unit cell angles spanning from $\phi = 0$ to $\phi = 0.5$, which is the range of angles present in Fig. 10.

The first three dispersion surfaces for $\phi = 0$ corresponding to out-of-plane modes are plotted over the first Brillouin zone in Fig. 11. Here, we nondimensionalize the frequency by defining $\omega_0 = h^{-1}\sqrt{E/\rho}$, where E and ρ are Young's modulus and mass density of the material that makes up the truss. As discussed in Zelhofer and Kochmann (2017), the lowest modes of planar beam networks are completely decoupled into in-plane and out-of-plane modes. That is, out-of-plane excitation will only excite out-of-plane

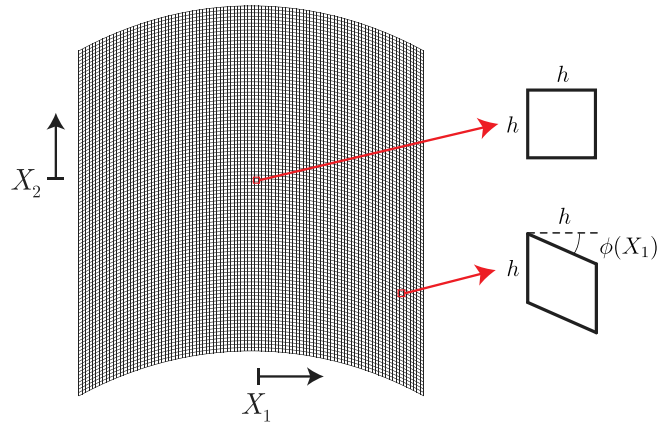


Fig. 10. Geometry of the graded beam network, with square unit cells at $X_1 = 0$ grading into parallelograms away from $X_1 = 0$, parameterized by the shear angle $\phi(X_1)$.

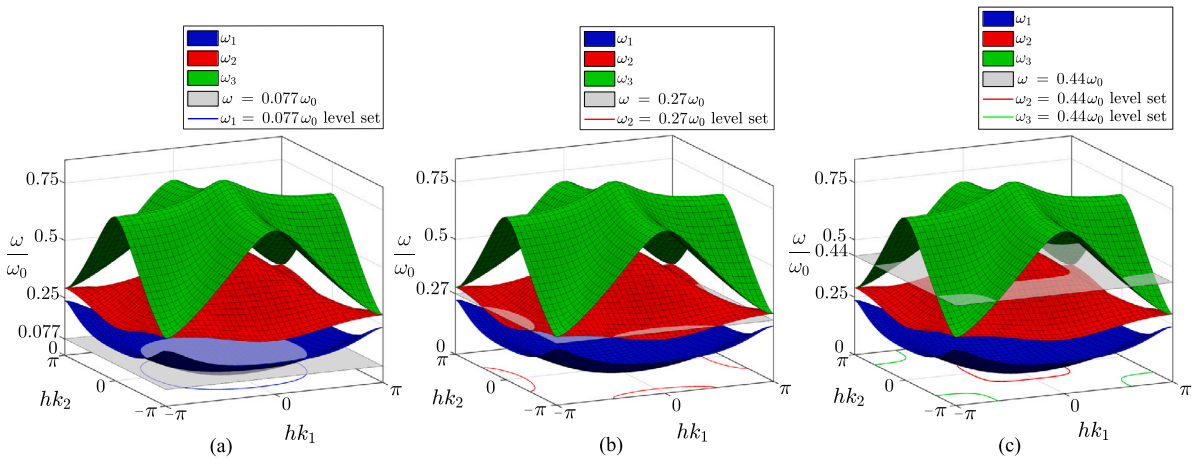


Fig. 11. Dispersion surfaces for the first three out-of-plane modes of the square unit cell at the excitation point $X_1 = X_2 = 0$. Ray tracing initial conditions correspond to the level set at the excitation frequency. Level sets for three excitation frequencies are shown: (a) $\omega = 0.077\omega_0$, (b) $\omega = 0.27\omega_0$, and (c) $\omega = 0.44\omega_0$.

modes and in-plane modes do not have to be considered. Initial conditions for ray tracing are obtained from the level sets of the dispersion surfaces at the excitation frequency. We present results corresponding to three representative excitation frequencies. The first excitation frequency is $\omega = 0.077\omega_0$, which excites only mode 1, as shown in Fig. 11a. The second is $\omega = 0.27\omega_0$, which excites only mode 2, as shown in Fig. 11b. Finally, $\omega = 0.44\omega_0$ excites modes 2 and 3, as shown in Fig. 11c.

From the pre-computed dispersion relations, finite differences are used to compute $\frac{\partial\omega}{\partial\mathbf{k}}$ and $\frac{\partial\omega}{\partial\phi}$, which are required for ray tracing. The spatial grading constant is used to compute the spatial derivative of the dispersion relation as $\frac{\partial\omega}{\partial X_1} = \frac{D}{h} \frac{\partial\omega}{\partial\phi}$, while $\frac{\partial\omega}{\partial X_2} = 0$. With the finite-difference derivatives in hand, the ray tracing procedure is identical to the previous mass-spring examples, following the steps of Section 3.6. Figs. 12a, 13a, 14a, and 14b show the resulting ray trajectories and amplitudes for the three excitation frequencies.

To verify the ray solutions, a transient dynamic finite element simulation is performed on a 100×100 grid of units, which corresponds to the domain plotted in Fig. 10. Each unit cell edge is modeled with 10 Timoshenko beam elements and the outer boundaries of the grid are clamped. A harmonic displacement with magnitude u_f is applied at the origin as an essential boundary condition. We apply a displacement rather than a force excitation, because out-of-plane harmonic forcing on a two-dimensional truss initially at rest may lead to a substantial transient response with parasitic low-frequency content. Displacement excitation, on the other hand, leads to much smaller transients (Zelhofer and Kochmann, 2017). To obtain the resulting excitation force F , which is required for comparison to ray amplitudes through Eq. (41), the amplitude of the steady-state reaction force at the origin from the finite element model is used.

Figs. 12, 13, and 14 show a comparison of the ray tracing and finite element solutions at each excitation frequency. In Figs. 12c, 13c, and 13d, the maximum displacement from ray theory is plotted, which has been interpolated onto the same points used in the finite element mesh. In Figs. 12b, 13b, and 14c, the maximum displacement amplitude during the finite element simulation is plotted. Finally, Figs. 12d, 13d, 14e compare the amplitudes along the X_2 -axis.

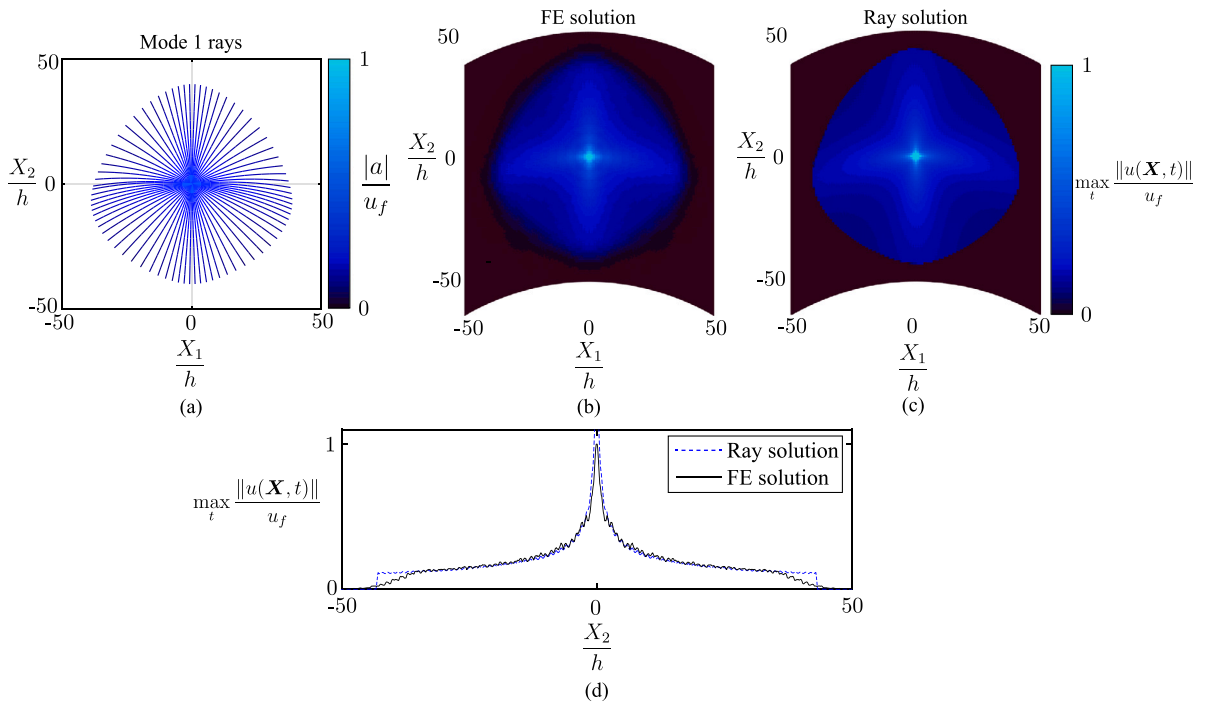


Fig. 12. Ray theory and finite element (FE) solutions for the graded truss example with excitation frequency $\omega_f = 0.077\omega_0$ at $t = 45/\omega_f$. (a) Mode 1 ray paths and amplitudes. (b) Maximum displacement amplitude from the FE solution. (c) Maximum displacement amplitude from the ray solution. (d) Comparison of the displacement amplitudes along the X_2 -axis (at $X_1 = 0$).

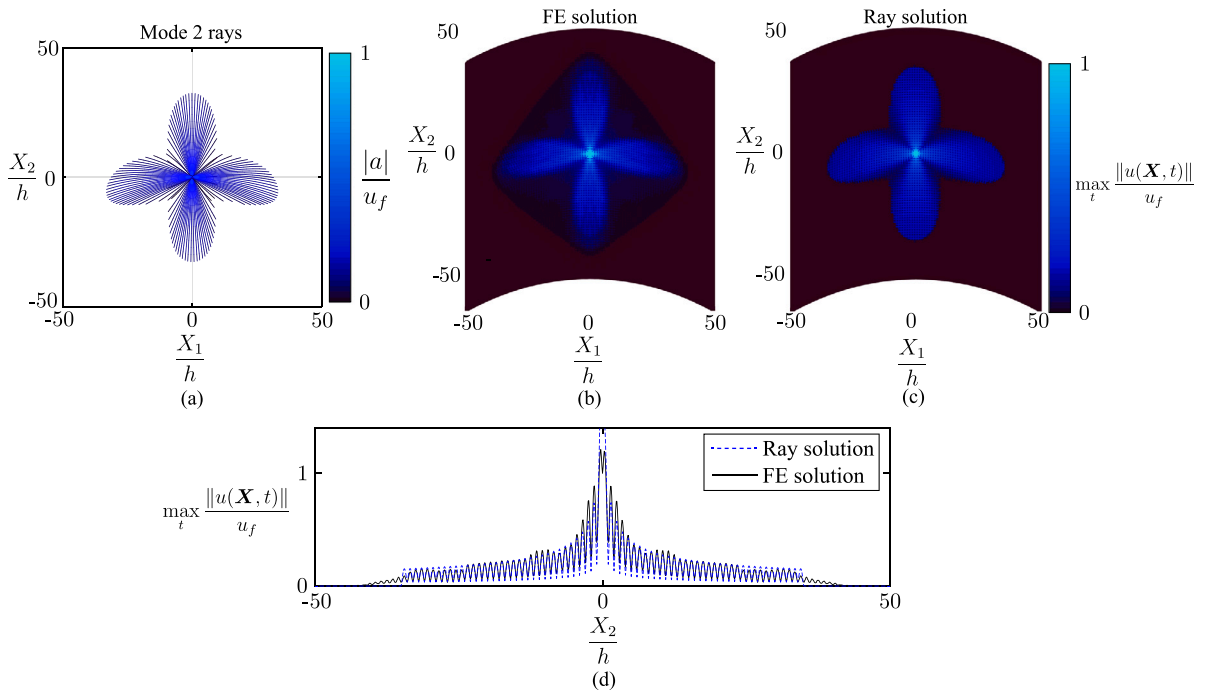


Fig. 13. Ray theory and finite element (FE) solutions for the graded truss example with excitation frequency $\omega_f = 0.27\omega_0$ at $t = 90/\omega_f$. (a) Mode 2 ray paths and amplitudes. (b) Maximum displacement amplitude from the FE solution. (c) Maximum displacement amplitude from the ray solution. (d) Comparison of the displacement amplitudes along the X_2 -axis (at $X_1 = 0$).

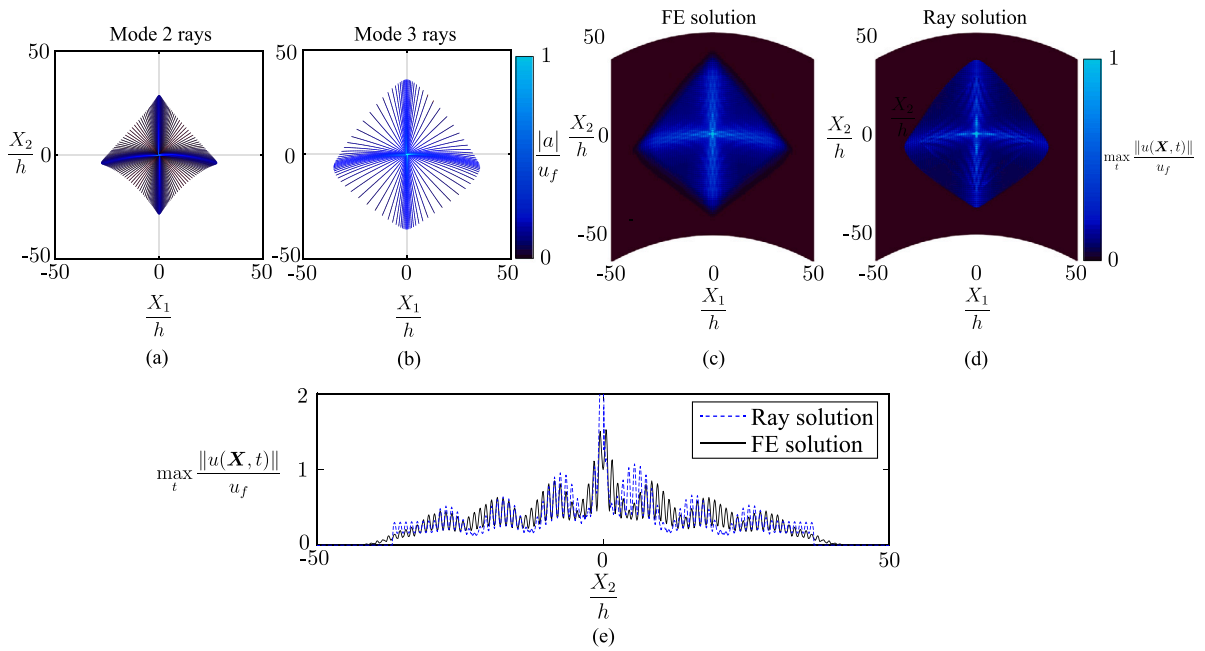


Fig. 14. Ray theory and finite element (FE) solutions for the graded truss example with excitation frequency $\omega_f = 0.44\omega_0$ at $t = 100/\omega_f$. (a) Mode 2 ray paths and amplitudes. (b) Mode 3 ray paths and amplitudes. (c) Maximum displacement amplitude from the FE solution. (d) Maximum displacement amplitude from the ray solution. (e) Comparison of the displacement amplitudes along the X_2 -axis (at $X_1 = 0$).

It is evident that the ray solution and the finite element solution closely agree, both in the location and shape of the wavefront as well as the amplitude for all three examples. No caustics are present in the ray solution in any of the examples, so the ray amplitude is valid everywhere except in the immediate vicinity of the point source. The oscillations in the amplitude observed in Figs. 12d and 13d are variations within each unit cell. The unit cell mode shape contributes to the displacement amplitude through Eq. (42), which causes amplitude variations within each unit. In Fig. 14e, oscillations are present within each unit cell, but interference between the two modes is also observed.

There are multiple reasons for the slight differences between the ray solution and finite element solution. In the finite element simulation, the truss is initially at rest; when the wave first arrives at a given point, there is a transient build up to the steady-state response. This is especially evident Fig. 12d near the wave front, where the finite element solution has not yet build up to steady state, so it exhibits a lower amplitude than ray theory, which only captures the steady-state response. Another consequence of the transient finite element analysis is that the harmonic displacement excitation is instantaneously switched on at $t = 0$, so frequencies other than the forcing frequency are inevitably excited. Finally, ray theory relies on the idealization of local periodicity, so the ray solutions are not exact.

The solutions for the three excitation frequencies also give insight into the difference between seismic ray theory and our theory. As discussed in Sections 3.2 and 3.3, seismic ray theory can be recovered by replacing unit cells with a homogenized effective material. Classical homogenization is valid in the low-frequency and long-wavelength (with respect to a unit cell) limit (Gonella and Ruzzene, 2008). In our example, only the first dispersion surface approaches the low-frequency limit. Therefore, seismic ray theory could approximate the (only slightly anisotropic) response at $\omega_f = 0.077\omega_0$ (Fig. 12), though the amplitude fluctuations within a unit cell could not be captured. However, the dispersive effects of the microstructure, which lead to the highly directional response in Figs. 13 and 14, corresponding to the second and third dispersion surfaces, cannot be captured by seismic ray theory, since they correspond to frequencies above the limit of validity of homogenization.

5. Conclusion

Spatially graded metamaterials have high potential for manipulating wave propagation in unprecedented ways. However, there is a lack of efficient modeling tools to explore the design space of graded metamaterials. To overcome this gap, we have developed ray theory for graded metamaterials, which offers an efficient and accurate means of modeling wave propagation. To this end, we assume local periodicity, so the material is considered to be periodic on a short length scale, while the unit cell is allowed to change on a long length scale. Under this assumption, ray theory has been derived based on an asymptotic analysis of the elastodynamic wave equation. Wave solutions are computed along ray trajectories that are obtained by solving a small first-order system of differential equations. Subsequently, the phase and amplitude of the waves along a ray are derived, from which an approximation of the displacement field can be obtained. Derivations of the ray solution parallel the well-established ray theory in seismology, though there are subtle differences in the underlying assumptions and the resulting ray tracing equations.

We demonstrated ray solutions on a series of examples. First, a mass–spring network with two modes was studied, for which analytical dispersion relations are available. In the periodic case, rays propagate along straight lines, while in the spatially graded case rays follow curved trajectories. Both the ray trajectories and amplitudes matched closely with the direct numerical solutions for a finite grid of masses, with the exception of caustics where the ray amplitude is singular. The final example considered a truss metamaterial modeled by beam finite elements. Such a model is physically realistic, at the cost of requiring the numerical evaluation of dispersion relations. Nevertheless, ray solutions were obtained based on numerical differentiation of the dispersion relation and were shown to agree closely with discrete finite element simulations.

The theoretical and numerical framework presented here provides an efficient means of exploring the design space of spatially graded metamaterials. There are many avenues for future research that can build upon this foundation. Due to its efficiency, ray theory also serves as a powerful basis for solving inverse problems in other fields (Lo and Inderwiesen, 1994), which provides inspiration for the inverse design of graded metamaterials.

CRedit authorship contribution statement

Charles Dorn: Conceptualization, Methodology, Software, Validation, Investigation, Data curation, Writing – original draft, Writing – review & editing. **Dennis M. Kochmann:** Conceptualization, Methodology, Writing – review & editing, Supervision.

Declaration of competing interest

The authors declare that they have no known competing financial interests or personal relationships that could have appeared to influence the work reported in this paper.

Data availability

Data will be made available on request.

Acknowledgments

This work was supported by an ETH Zürich Postdoctoral Fellowship, Switzerland. The authors thank Bastian Telgen for providing the finite element code to compute dispersion relations for the truss metamaterial example, which is available at https://gitlab.ethz.ch/mechanics-and-materials/ae108/-/releases/v0.1.0-dispersion_relation.

Appendix A. Derivation of leading-order asymptotics

This appendix derives the leading-order asymptotic terms of the elastodynamic wave equation, Eq. (1). We first modify the elastodynamic wave equation to account for the two length scales of interest. Noting that $\frac{\partial}{\partial x} = \frac{\partial}{\partial X} + \epsilon^{-1} \frac{\partial}{\partial y}$, Eq. (1) becomes

$$\rho \ddot{u}_i = \underbrace{(C_{ijkl} u_{k,X_l})_{,X_j}}_{=S_1} + \underbrace{\epsilon^{-1} (C_{ijkl} u_{k,y_l})_{,X_j}}_{=S_2} + \underbrace{\epsilon^{-1} (C_{ijkl} u_{k,X_l})_{,y_j}}_{=S_3} + \underbrace{\epsilon^{-2} (C_{ijkl} u_{k,y_l})_{,y_j}}_{=S_4}. \quad (\text{A.1})$$

Upon inserting the ansatz of Eq. (7) into Eq. (A.1), and applying the assumptions of local periodicity from Eqs. (6) and (9), the four terms become

$$\begin{aligned} S_1 &= \hat{C}_{ijkl, X_j} (A_{k,X_l} + \epsilon^{-1} i A_k k_l) e^{i\varphi/\epsilon} + \hat{C}_{ijkl} \left[(A_{k,X_l} + \epsilon^{-1} i A_k k_l) \epsilon^{-1} i k_j + A_{k,X_j X_l} + A_{k,X_j} \epsilon^{-1} i k_l + A_k \epsilon^{-1} i k_{l,X_j} \right] e^{i\varphi/\epsilon} + O(\epsilon^0) \\ &= \epsilon^{-2} (-\hat{C}_{ijkl} \hat{A}_k k_l k_j) e^{i\varphi/\epsilon} + \epsilon^{-1} i \left[\hat{C}_{ijkl} (\hat{A}_{k,X_j} k_l + \hat{A}_{k,X_l} k_j + \hat{A}_k k_{l,X_j}) \right] e^{i\varphi/\epsilon} + O(\epsilon^0), \end{aligned} \quad (\text{A.2})$$

$$\begin{aligned} S_2 &= \epsilon^{-1} \hat{C}_{ijkl, X_j} A_{k,y_l} e^{i\varphi/\epsilon} + \epsilon^{-1} \hat{C}_{ijkl} (A_{k,y_l X_j} + \epsilon^{-1} i A_{k,X_l} k_j) e^{i\varphi/\epsilon} + O(\epsilon^0) \\ &= \epsilon^{-2} \hat{C}_{ijkl} \hat{A}_{k,y_l} i k_j e^{i\varphi/\epsilon} + \epsilon^{-1} \hat{C}_{ijkl} \hat{A}_{k,y_l X_j} e^{i\varphi/\epsilon} + O(\epsilon^0), \end{aligned} \quad (\text{A.3})$$

$$\begin{aligned} S_3 &= \epsilon^{-1} \left[\hat{C}_{ijkl, y_j} (A_{k,X_l} + \epsilon^{-1} i A_k k_l) + \hat{C}_{ijkl} (A_{k,X_l y_j} + \epsilon^{-1} i A_{k,y_j} k_l) \right] e^{i\varphi/\epsilon} + O(\epsilon^0) \\ &= \epsilon^{-2} i \left(\hat{C}_{ijkl, y_j} \hat{A}_k k_l + \hat{C}_{ijkl} \hat{A}_{k,y_j} k_l \right) e^{i\varphi/\epsilon} + \epsilon^{-1} \left(\hat{C}_{ijkl, y_j} \hat{A}_{k,X_l} + \hat{C}_{ijkl} \hat{A}_{k,X_l y_j} \right) e^{i\varphi/\epsilon} + O(\epsilon^0), \end{aligned} \quad (\text{A.4})$$

$$\begin{aligned} S_4 &= \epsilon^{-2} \left(C_{ijkl, y_j} A_{k,y_l} + C_{ijkl} A_{k,y_l y_j} \right) e^{i\varphi/\epsilon} \\ &= \epsilon^{-2} \left(\hat{C}_{ijkl, y_j} \hat{A}_{k,y_l} + \hat{C}_{ijkl} \hat{A}_{k,y_l y_j} \right) e^{i\varphi/\epsilon} + O(\epsilon^0). \end{aligned} \quad (\text{A.5})$$

Collecting all terms of order ϵ^{-2} , we define the leading order term L as

$$L_i = \hat{C}_{ijkl} (-\hat{A}_k k_j k_l + i \hat{A}_{k,y_l} k_j + i \hat{A}_{k,y_j} k_l + \hat{A}_{k,y_j y_l}) + \hat{C}_{ijkl, y_j} (\hat{A}_{k,y_l} + i \hat{A}_k k_l) + \omega^2 \hat{\rho} \hat{A}_i. \quad (\text{A.6})$$

Similarly, collecting all terms of order ϵ^{-1} , we define the second leading term M as

$$M_i = \hat{C}_{ijkl} (i \hat{A}_{k,X_j} k_l + i \hat{A}_{k,X_l} k_j + \hat{A}_{k,X_j y_l} + \hat{A}_{k,X_l y_j} + i \hat{A}_k k_{l,X_j}) + \hat{C}_{ijkl, y_j} \hat{A}_{k,X_l}. \quad (\text{A.7})$$

These two leading terms define the asymptotic elastodynamic equation, Eq. (10), from which ray theory is derived. In L and M , only the periodic parts of the amplitude, \hat{A} , and the material properties, \hat{C} and $\hat{\rho}$, are present due to our assumption that the non-periodic perturbation terms in Eqs. (6) and (9) are of order ϵ^2 . If perturbations of order ϵ were considered instead, then \tilde{C} , $\tilde{\rho}$, and \tilde{A} would appear in M . By restricting the perturbations to order ϵ^2 , the amplitude derivations of Sections Section 3.3, 3.4, and 3.5 take the simplest possible form, while also providing accurate results, as demonstrated in Section 4.

Appendix B. An alternative expression for the group velocity

In this section, we use the leading order term of the asymptotic elastodynamic equation to derive an expression for the group velocity, which is required for the derivation of the transport equation in Section 3.3. Differentiating Eq. (13) with respect to k_q , we obtain

$$2\hat{\rho}\omega \frac{\partial\omega}{\partial k_q} \hat{A}_i = -i\hat{C}_{ijkl,y_j} \delta_{ql} \hat{A}_k - \hat{C}_{ijkl} \left(i\delta_{ql} \hat{A}_{k,y_j} + i\delta_{qj} \hat{A}_{k,y_l} - k_j \delta_{ql} \hat{A}_k - k_l \delta_{qj} \hat{A}_k \right), \tag{B.1}$$

where δ is the Kronecker delta. By inserting the modal amplitude of Eq. (19) and the definition of the group velocity in Eq. (5), and multiplying both sides of the equation by g_i , we arrive at

$$2\hat{\rho}\omega V_q a g_i g_i = -i\hat{C}_{ijkl,y_j} \delta_{ql} a g_k g_i - \hat{C}_{ijkl} \left(i\delta_{ql} a g_{k,y_j} g_i + i\delta_{qj} a g_{k,y_l} g_i - k_j \delta_{ql} a g_k g_i - k_l \delta_{qj} a g_k g_i \right). \tag{B.2}$$

Note that, here, a is a function of X only, so its derivative with respect to y vanishes. Dividing both sides by a and utilizing the symmetry of the elasticity tensor ($\hat{C}_{ijkl} = \hat{C}_{klij}$), the above becomes

$$2\hat{\rho}g^2 \omega V_l = -i(\hat{C}_{ijkl} g_i g_k)_{,y_j} + 2\hat{C}_{ijkl} k_j g_i g_k, \tag{B.3}$$

where $g^2 = g_i g_i$. Finally, by re-arranging, we arrive at the simple expression for the group velocity:

$$V_l = -\frac{i}{2\hat{\rho}\omega g^2} (\hat{C}_{ijkl} g_i g_k)_{,y_j} + \frac{1}{\hat{\rho}\omega g^2} \hat{C}_{ijkl} k_j g_i g_k. \tag{B.4}$$

This result differs from the analogous identity in seismic ray theory for the group velocity in a ‘‘locally homogeneous’’ solid, which is $V_l^s = \rho^{-1} \omega^{-1} C_{ijkl} k_j g_i g_k$ (Cerveny, 2001). In Eq. (B.4) there is an additional term, highlighting the difference between locally periodic material and a locally homogeneous material. Despite this difference, the ray tracing Eqs. (17) and transport Eq. (23) are identical between locally periodic ray theory and seismic ray theory. However, one must be careful in comparing the two contexts. Seismic ray theory relies on the commonly used identity $k \cdot V^s = \omega$, which does not apply to locally periodic material.

Appendix C. Derivation of the point source amplitude

The constant ψ_0 , which is originally defined in Eq. (32), is required for the computation of ray amplitudes due to a point excitation. The form of ψ_0 in Eq. (37) contains the quotient of J and Z , which both tend to zero as the point source is approached. We show that J and Z tend to zero at the same rate so that their quotient, as the point source is approached, is a finite constant.

The unit tangent vector of a ray is $\frac{\partial X}{\partial s} = V/V$, which allows the definition of the ray Jacobian in Eq. (24) to be rewritten as

$$J = \frac{\partial X_i}{\partial \gamma} \epsilon_{ij} V^{-1} V_j, \tag{C.1}$$

where ϵ_{ij} is the 2D Levi-Civita symbol, which has components $\epsilon_{12} = 1$, $\epsilon_{21} = -1$, and $\epsilon_{11} = \epsilon_{22} = 0$. Differentiating Eq. (17a) with respect to γ and noting that $\frac{\partial\omega}{\partial X}$ is negligible in the limit as the point source is approached, we obtain

$$\frac{\partial}{\partial \gamma} \frac{\partial X_i}{\partial t} = \frac{\partial^2 \omega}{\partial k_i \partial \gamma} \tag{C.2}$$

or

$$\frac{\partial}{\partial t} \frac{\partial X_i}{\partial \gamma} = \frac{\partial^2 \omega}{\partial k_i \partial k_j} \frac{\partial k_j}{\partial \gamma}. \tag{C.3}$$

For small values of t ,

$$\frac{\partial X_i}{\partial \gamma} \approx \frac{\partial^2 \omega}{\partial k_i \partial k_j} \frac{\partial k_j}{\partial \gamma} t. \tag{C.4}$$

Inserting Eq. (C.4) into Eq. (C.1), as the point source is approached along the ray, the Jacobian takes the form

$$J_0 = \lim_{t \rightarrow 0^+} J = \lim_{t \rightarrow 0^+} \frac{t}{V_0} \frac{\partial^2 \omega}{\partial k_i \partial k_j} \frac{\partial k_j}{\partial \gamma} \epsilon_{ik} V_{0k}. \tag{C.5}$$

The corresponding sign of J_0 as the point source is approached along the ray, since t is positive, is

$$\text{sgn}(J_0) = \text{sgn} \left(\frac{\partial^2 \omega}{\partial k_i \partial k_j} \Big|_0 \frac{\partial k_j}{\partial \gamma} \Big|_0 \epsilon_{ik} V_{0k} \right), \tag{C.6}$$

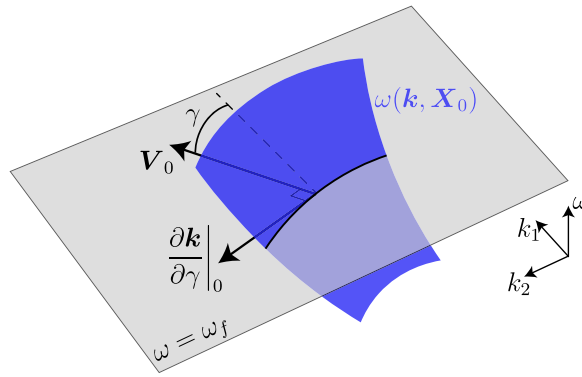


Fig. C.1. Schematic of a portion of a dispersion surface (in blue) at the forcing location X_0 with the level set at forcing frequency ω_f highlighted (solid black line).

where $|_0$ denotes evaluation of the derivatives at the location of the point source, taken as $X_0 = 0$, and at the initial condition for the wave vector k_0 of the given ray.

To take the limit of Z as the point source is approached along a ray, we first rewrite the definition of Z from Eq. (36) in the form

$$Z = X_i \epsilon_{ji} \frac{\partial^2 \omega}{\partial k_j \partial k_l} \epsilon_{lm} V_m. \tag{C.7}$$

In the limit $t \rightarrow 0^+$ we have $X_i \approx \frac{dX_i}{dt} t = V_i t$, so that

$$Z_0 = \lim_{t \rightarrow 0^+} Z = \lim_{t \rightarrow 0^+} t V_i \epsilon_{ji} \frac{\partial^2 \omega}{\partial k_j \partial k_l} \epsilon_{lm} V_m. \tag{C.8}$$

The sign of Z_0 , which is required for the computation of ray amplitudes from a point source, follows as

$$\text{sgn}(Z_0) = \text{sgn} \left(V_{0i} \epsilon_{ji} \frac{\partial^2 \omega}{\partial k_j \partial k_l} \Big|_0 \epsilon_{lm} V_{0m} \right). \tag{C.9}$$

To evaluate the quotient of J_0 and Z_0 , using Eqs. (C.5) and (C.8) we obtain

$$\frac{J_0}{Z_0} = \frac{V_0^{-1} \frac{dk_n}{d\gamma} Q_n}{\epsilon_{ji} V_{0j} Q_i}. \tag{C.10}$$

To simplify the derivation, vector Q is defined as

$$Q_i = \frac{\partial^2 \omega}{\partial k_i \partial k_m} \Big|_0 \epsilon_{ml} V_{0l}. \tag{C.11}$$

Eq. (C.10) is independent of t , so the quotient J_0/Z_0 is finite as the point source is approached, despite J_0 and Z_0 being singular.

Since γ parameterizes rays of the excitation frequency, $\frac{\partial k}{\partial \gamma} \Big|_0$ is tangent to the excitation frequency level set of the dispersion surface. Therefore, it is perpendicular to V_0 , which is the gradient of the dispersion surface, so we can write $\frac{\partial k}{\partial \gamma} \Big|_0 = \left\| \frac{\partial k}{\partial \gamma} \Big|_0 \right\| V_0^\perp$. Here, V_0^\perp is defined as a unit tangent vector to the level set of the initial dispersion surface (which is normal to the group velocity at the point source). Fig. C.1 illustrates vectors V_0 and $\frac{\partial k}{\partial \gamma} \Big|_0$. Additionally, the vector $\epsilon_{ij} V_{0j}$ is perpendicular to the ray and can be written as $\epsilon_{ij} V_{0j} = V V_0^\perp$. Therefore,

$$\left| \frac{J_0}{Z_0} \right| = \frac{\left\| \frac{\partial k}{\partial \gamma} \Big|_0 \right\| V_0^\perp \cdot Q}{V_0^2 V_0^\perp \cdot Q} = V_0^{-2} \left\| \frac{\partial k}{\partial \gamma} \Big|_0 \right\|. \tag{C.12}$$

Inserting Eq. (C.12) into Eq. (37), the final form of the constant ψ_0 is

$$\psi_0 = \frac{i F^T g_0 \sqrt{\text{sgn}(J_0)}}{2\omega \sqrt{2\pi} V_0} \left\| \frac{\partial k}{\partial \gamma} \Big|_0 \right\|^{1/2} e^{-i \frac{\pi}{4} \text{sgn}(Z_0)}. \tag{C.13}$$

Appendix D. Mass-spring network dispersion relations

To derive the dispersion relations of the mass-spring networks in Figs. 3 and 7, we begin by formulating the equations of motion for a single mass. The length of the unit cell diagonal is $L = \sqrt{h_1^2 + h_2^2}$ and the angle of the diagonal is $\theta = \tan^{-1}(h_2/h_1)$.

Assuming small displacements, summing the forces of all springs connected to mass i, j yields the equation of motion

$$\begin{aligned}
 m \begin{bmatrix} \ddot{u}_1^{i,j} \\ \ddot{u}_2^{i,j} \end{bmatrix} &= K(u_1^{i+1,j} - u_1^{i,j}) \begin{bmatrix} 1 \\ 0 \end{bmatrix} + K(-u_1^{i-1,j} + u_1^{i,j}) \begin{bmatrix} -1 \\ 0 \end{bmatrix} \\
 &+ K(u_2^{i,j+1} - u_2^{i,j}) \begin{bmatrix} 0 \\ 1 \end{bmatrix} + K(-u_2^{i,j-1} + u_2^{i,j}) \begin{bmatrix} 0 \\ -1 \end{bmatrix} \\
 &+ K \left(h_1(u_1^{i+1,j+1} - u_1^{i,j}) + h_2(u_2^{i+1,j+1} - u_2^{i,j}) \right) L^{-1} \begin{bmatrix} \cos \theta \\ \sin \theta \end{bmatrix} \\
 &+ K \left(h_1(-u_1^{i-1,j-1} + u_1^{i,j}) + h_2(-u_2^{i-1,j-1} + u_2^{i,j}) \right) L^{-1} \begin{bmatrix} -\cos \theta \\ -\sin \theta \end{bmatrix} \\
 &+ K \left(h_1(u_1^{i+1,j-1} - u_1^{i,j}) + h_2(-u_2^{i+1,j-1} + u_2^{i,j}) \right) L^{-1} \begin{bmatrix} \cos \theta \\ -\sin \theta \end{bmatrix} \\
 &+ K \left(h_1(-u_1^{i-1,j+1} + u_1^{i,j}) + h_2(u_2^{i-1,j+1} - u_2^{i,j}) \right) L^{-1} \begin{bmatrix} -\cos \theta \\ \sin \theta \end{bmatrix}.
 \end{aligned} \tag{D.1}$$

If $h_1 = h_2$, these equations of motion simplify to those presented by Jensen (2003). To perform direct numerical simulations on a finite mass-spring network, Eq. (D.1) is used to extract the mass and stiffness matrices.

Based on the equation of motion for a single mass, which represents one unit cell for the chosen networks, dispersion relations are derived by assuming that the network is y -periodic and applying Bloch boundary conditions. This leads to displacements of the form

$$\mathbf{u}^{ij} = \begin{bmatrix} A_1^{ij} \\ A_2^{ij} \end{bmatrix} e^{i(\mathbf{k} \cdot \mathbf{y} - \omega t)} = \begin{bmatrix} A_1^{ij} \\ A_2^{ij} \end{bmatrix} e^{i(h_1 k_1 i + h_2 k_2 j)} e^{-i\omega t}. \tag{D.2}$$

Inserting Eq. (D.2) into Eq. (D.1) and simplifying leads to the following eigenvalue problem:

$$\left(\begin{bmatrix} \alpha & \beta \\ \beta & \eta \end{bmatrix} - \omega^2 \mathbf{I} \right) \mathbf{A} = \mathbf{0}, \tag{D.3}$$

where

$$\begin{aligned}
 \alpha &= \frac{2K}{Lm} [1 - \cos(h_1 k_1 + h_2 k_2)] h_1 \cos \theta + \frac{2K}{Lm} [1 - \cos(h_1 k_1 - h_2 k_2)] h_1 \cos \theta + \frac{2K}{m} [1 - \cos(h_1 k_1)], \\
 \beta &= \frac{2K}{Lm} [1 - \cos(h_1 k_1 + h_2 k_2)] h_1 \sin \theta - \frac{2K}{Lm} [1 - \cos(h_1 k_1 - h_2 k_2)] h_2 \cos \theta, \\
 \eta &= \frac{2K}{Lm} [1 - \cos(h_1 k_1 + h_2 k_2)] h_2 \sin \theta + \frac{2K}{Lm} [1 - \cos(h_1 k_1 - h_2 k_2)] h_2 \sin \theta + \frac{2K}{m} [1 - \cos(h_2 k_2)].
 \end{aligned} \tag{D.4}$$

The eigenvalues of the 2×2 matrix in Eq. (D.3) are available analytically. This results in a set of analytical dispersion relations for the two frequencies ω_1 and ω_2 of the mass spring network, given by

$$\begin{aligned}
 \omega_1^2 &= \frac{1}{2} \left(\alpha + \eta - \sqrt{(\alpha - \eta)^2 + 4\beta^2} \right) \\
 \omega_2^2 &= \frac{1}{2} \left(\alpha + \eta + \sqrt{(\alpha - \eta)^2 + 4\beta^2} \right).
 \end{aligned} \tag{D.5}$$

For the case of the spatially graded mass-spring network, these represent the local dispersion relations under the assumption of local periodicity.

References

Aguzzi, G., Kanellopoulos, C., Wiltshaw, R., Craster, R.V., Chatzi, E.N., Colombi, A., 2022. Octet lattice-based plate for elastic wave control. *Sci. Rep.* 12 (1), 1–14.

Allaire, G., Palombaro, M., Rauch, J., 2011. Diffractive geometric optics for Bloch wave packets. *Arch. Ration. Mech. Anal.* 202 (2), 373–426.

Alshaqaq, M., Sugino, C., Erturk, A., 2022. Programmable rainbow trapping and band-gap enhancement via spatial group-velocity tailoring in elastic metamaterials. *Phys. Rev. A* 17 (2).

Authier, A., 2004. *Dynamical Theory of X-Ray Diffraction*, Vol. 11. Oxford University Press.

Banerjee, A., Das, R., Calius, E.P., 2017. Frequency graded 1D metamaterials: A study on the attenuation bands. *J. Appl. Phys.* 122 (7).

Ben-Menahem, A., 1995. A concise history of mainstream seismology: Origins, legacy, and perspectives. *Bull. Seismol. Soc. Am.* 85 (4), 1202–1225.

Bensoussan, A., Lions, J.-L., Papanicolaou, G., 1978. *Asymptotic Analysis for Periodic Structures*. American Mathematical Soc.

Berry, M.V., Mount, K., 1972. Semiclassical approximations in wave mechanics. *Rep. Progr. Phys.* 35 (1), 315.

Bleistein, N., 2012. *Mathematical Methods for Wave Phenomena*. Academic Press.

Bloch, F., 1929. Über die quantenmechanik der elektronen in kristallgittern. *Z. Phys.* 52 (7), 555–600.

Born, M., Wolf, E., 2013. *Principles of Optics: Electromagnetic Theory of Propagation, Interference and Diffraction of Light*. Elsevier.

Brillouin, L., 1953. *Wave Propagation in Periodic Structures: Electric Filters and Crystal Lattices*, Vol. 2. Dover Publications.

Cassan, E., Do, K.-V., 2011. Analytic design of graded photonic crystals in the metamaterial regime. *J. Opt. Soc. Amer. B* 28 (8), 1905–1910.

Cassan, E., Do, K.-V., Caer, C., Marris-Morini, D., Vivien, L., 2011. Short-wavelength light propagation in graded photonic crystals. *J. Lightwave Technol.* 29 (13), 1937–1943.

Cervený, V., 2001. *Seismic Ray Theory*. Cambridge University Press.

- Chaplain, G.J., De Ponti, J.M., Colombi, A., Fuentes-Dominguez, R., Dryburg, P., Pieris, D., Smith, R.J., Clare, A., Clark, M., Craster, R.V., 2020a. Tailored elastic surface to body wave umklapp conversion. *Nature Commun.* 11 (1), 1–6.
- Chaplain, G.J., Pajer, D., De Ponti, J.M., Craster, R., 2020b. Delineating rainbow reflection and trapping with applications for energy harvesting. *New J. Phys.* 22 (6).
- Chapman, C., 2004. *Fundamentals of Seismic Wave Propagation*. Cambridge University Press.
- Chen, Y., Nassar, H., Huang, G., 2021. Discrete transformation elasticity: An approach to design lattice-based polar metamaterials. *Internat. J. Engrg. Sci.* 168.
- Cherednichenko, K., 2018. Two-scale series expansions for travelling wave packets in one-dimensional periodic media. *arXiv preprint arXiv:1802.05809*.
- Colquitt, D., Craster, R., Makwana, M., 2015. High frequency homogenisation for elastic lattices. *Q. J. Mech. Appl. Math.* 68 (2), 203–230.
- Craster, R.V., Kaplunov, J., Pichugin, A.V., 2010. High-frequency homogenization for periodic media. *Proc. Royal Soc. A* 466 (2120), 2341–2362.
- De Ponti, J.M., 2021. *Graded Elastic Metamaterials for Energy Harvesting*. Springer.
- Gonella, S., Ruzzene, M., 2008. Homogenization and equivalent in-plane properties of two-dimensional periodic lattices. *Int. J. Solids Struct.* 45 (10), 2897–2915.
- Hamilton, W.R., 1828. Theory of systems of rays. *Trans. Royal Ir. Acad.* 15, 69–174.
- Hussein, M.I., Leamy, M.J., Ruzzene, M., 2014. Dynamics of phononic materials and structures: Historical origins, recent progress, and future outlook. *Appl. Mech. Rev.* 66 (4).
- Isaacson, R.A., 1968. Gravitational radiation in the limit of high frequency. I. The linear approximation and geometrical optics. *Phys. Rev.* 166 (5), 1263.
- Jensen, J.S., 2003. Phononic band gaps and vibrations in one- and two-dimensional mass-spring structures. *J. Sound Vib.* 266 (5), 1053–1078.
- Jensen, F.B., Kuperman, W.A., Porter, M.B., Schmidt, H., Tolstoy, A., 2011. *Computational Ocean Acoustics*, Vol. 794. Springer.
- Jiao, Y., Fan, S., Miller, D.A., 2004. Designing for beam propagation in periodic and nonperiodic photonic nanostructures: Extended Hamiltonian method. *Phys. Rev. E* 70 (3).
- Kadic, M., Wegener, M., Nicolet, A., Zolla, F., Guenneau, S., Diatta, A., 2020. Elastodynamic behavior of mechanical cloaks designed by direct lattice transformations. *Wave Motion* 92.
- Kato, N., 1963. Pendellösung fringes in distorted crystals I. Fermat's principle for Bloch waves. *J. Phys. Soc. Japan* 18 (12), 1785–1791.
- Kendall, J., Guest, W., Thomson, C., 1992. Ray-theory Green's function reciprocity and ray-centred coordinates in anisotropic media. *Geophys. J. Int.* 108 (1), 364–371.
- Langley, R.S., 1996. The response of two-dimensional periodic structures to point harmonic forcing. *J. Sound Vib.* 197 (4), 447–469.
- Liu, C., Du, Z., Zhang, W., Zhu, Y., Guo, X., 2017. Additive manufacturing-oriented design of graded lattice structures through explicit topology optimization. *J. Appl. Mech.* 84 (8).
- Lo, T.-W., Inderwiesien, P.L., 1994. *Fundamentals of Seismic Tomography*. Society of Exploration Geophysicists.
- Lustig, B., Elbaz, G., Muhafra, A., Shmuel, G., 2019. Anomalous energy transport in laminates with exceptional points. *J. Mech. Phys. Solids* 133.
- Mazzotti, M., Gupta, M., Santangelo, C., Ruzzene, M., 2022. Elastic wave manipulation in geodesic lenses. *arXiv preprint arXiv:2203.08266*.
- Mohammadi, S., Adibi, A., 2011. On chip complex signal processing devices using coupled phononic crystal slab resonators and waveguides. *AIP Adv.* 1 (4).
- Nassar, H., Chen, Y., Huang, G., 2019. Isotropic polar solids for conformal transformation elasticity and cloaking. *J. Mech. Phys. Solids* 129, 229–243.
- Nolde, E., Craster, R., Kaplunov, J., 2011. High frequency homogenization for structural mechanics. *J. Mech. Phys. Solids* 59 (3), 651–671.
- Norris, A., Rebinsky, D., 1994. Membrane and flexural waves on thin shells. *J. Vib. Acoust.* 116.
- Panesar, A., Abdi, M., Hickman, D., Ashcroft, I., 2018. Strategies for functionally graded lattice structures derived using topology optimisation for additive manufacturing. *Addit. Manuf.* 19, 81–94.
- Phani, A.S., Hussein, M.I., 2017. *Dynamics of Lattice Materials*. John Wiley & Sons.
- Pierce, A.D., 1970. Physical interpretation of the WKB or eikonal approximation for waves and vibrations in inhomogeneous beams and plates. *J. Acoust. Soc. Am.* 48 (1B), 275–284.
- Russell, P., Birks, T., 1996. Bloch wave optics in photonic crystals: Physics and applications. In: *Photonic Band Gap Materials*. Springer, pp. 71–91.
- Russell, P.S.J., Birks, T., 1999. Hamiltonian optics of nonuniform photonic crystals. *J. Lightwave Technol.* 17 (11).
- Sanders, E., Pereira, A., Paulino, G., 2021. Optimal and continuous multilattice embedding. *Sci. Adv.* 7 (16).
- Schnitzer, O., 2017. Waves in slowly varying band-gap media. *SIAM J. Appl. Math.* 77 (4), 1516–1535.
- Srivastava, A., Willis, J.R., 2017. Evanescent wave boundary layers in metamaterials and sidestepping them through a variational approach. *Proc. Royal Soc. A* 473 (2200).
- Telgen, B., Sigmund, O., Kochmann, D.M., 2022. Topology optimization of graded truss lattices based on on-the-fly homogenization. *J. Appl. Mech.* 89 (6).
- Thorne, K.S., Blandford, R.D., 2017. *Modern Classical Physics: Optics, Fluids, Plasmas, Elasticity, Relativity, and Statistical Physics*. Princeton University Press.
- Trainiti, G., Rimoli, J.J., Ruzzene, M., 2016. Wave propagation in undulated structural lattices. *Int. J. Solids Struct.* 97, 431–444.
- Trainiti, G., Rimoli, J.J., Ruzzene, M., 2018. Optical evaluation of the wave filtering properties of graded undulated lattices. *J. Appl. Phys.* 123 (9), 091706.
- Wang, D.-F., Wang, Y.-Q., Qian, Z.-H., Tachi, T., Chuang, K.-C., 2021. A graded miura-ori phononic crystals lens. *Phys. Lett. A* 418.
- Willis, J.R., 2016. Negative refraction in a laminate. *J. Mech. Phys. Solids* 97, 10–18.
- Zelhofer, A.J., Kochmann, D.M., 2017. On acoustic wave beaming in two-dimensional structural lattices. *Int. J. Solids Struct.* 115, 248–269.